TECHNOLOGICAL EDUCATIONAL INSTITUTE OF CRETE

SCHOOL OF APPLIED SCIENCE

Department of Environmental and Natural Resources Engineering - Chania

Laboratory: Laboratory of Geophysics and Seismology

BACHELOR THESIS:

Monitoring Land Surface Temperature in the Aegean Volcanic Arc using Remote Sensing Techniques and MODIS – LST imagery

student

PELELI SOFIA

Supervisor(s) – Professor(s)

Dr. Kouli Maria – Laboratory Instructor

CHANIA 2016

~ 1 ~

UNESCO Chair
SOLID EARTH PHYSICS and GEOHAZARDS RISK REDUCTION
Technological Educational Institute of Crete, Greece
Head of the Chair, Dr. Filippos Vallianatos
Professor of Geophysics & Seismology
3 Romanou Str., Chania, GR 73100, Crete, Greece. email : fvallian@chania.teicrete.gr

To my friends and family

ΕΞΕΤΑΣΤΙΚΗ ΕΠΙΤΡΟΠΗ

1. Εξεταστής

2. Εξεταστής

3. Εξεταστής

ΠΕΡΙΛΗΨΗ

Το Αιγαίο Πέλαγος αποτελείται από νησιά με ισχυρή γεωθερμική δραστηριότητα εξαιτίας της ηφαιστειότητας που υπάρχει στο Αιγαιακό Ηφαιστειακό Τόξο. Το προιόν Land Surface Temperature (LST) του καταγραφικού συστήματος Moderate Resolution Imaging Spectro-radiometer (MODIS) χρησιμοποιείται για πρώτη φορά με σκοπό την αποτύπωση και την χαρτογράφηση πιθανής έξαρσης της ηφαιστειακής/γεωθερμικής δραστηριότητας στα ήδη γνωστά ηφαιστειακά/γεωθερμικά πεδία. Η καινοτομία που εφαρμόστηκε σε αυτή την πτυχιακή εργασία είναι η εφαρμογή της τεχνικής RST (Robust Satellite Technique), μίας στατιστικής μεθόδου απαλοιφής του θορύβου από τα δεδομένα και ενίσχυσης του σήματος για την καλύτερη ανίχνευσή του και άρα για καλύτερης ποιότητας αποτελέσματα. Τα δεδομένα καλύπτουν μια χρονική περίοδο 12 ετών (2003-2014) και αφορούν σε ημερήσιες εικόνες. Αρχικά, ο δείκτης ALICE χρησιμοποιείται για τον καθορισμό των ανώμαλων TIR εικονοστοιχείων σε μηνιαίο και στη συνέχεια σε ημερήσιο χρονικό παράθυρο. Ακολούθως, εφαρμόζεται ο δείκτης RETIRA προκειμένου να εξαληφθούν οι επιδράσεις των κλιματικών συνθηκών. Οι δείκτες εφαρμόστηκαν σε περιβάλλον ΓΣΠ όπου αναπτύχθηκαν νέα εργαλεία μέσω του περιβάλλοντος εργασίας Model Builder. Οι εντονότερες θερμικές ανωμαλίες εντοπίζονται στα νησιά Λέσβος, Χίος, Κως, Σάμος, Ικαρία, Νίσυρος και Σαντορίνη με τα 5 πρώτα να εμφανίζουν ανωμαλίες μεγάλης συχνότητας και διάρκειας. Οι κυριότερες ανωμαλίες εμφανίζονται από Απρίλιο μέχρι Οκτώβριο, ενώ τους υπόλοιπους μήνες εμφανίζονται κυρίως ψευδώς θετικές ανωμαλίες λόγω της υψηλής νεφοκάλυψης. Στις περισσότερες των περιπτώσεων, οι ανωμαλίες αυτές δεν φαίνεται να σχετίζονται με φαινόμενα όπως η σεισμικότητα και οι δασικές φωτιές. Χαρακτηριστικά τον Οκτώβριο του 2013 έχουμε μία χρονοσειρά ανωμαλιών 24 ημερών (4/11-28/11) στα νησιά των Δωδεκανήσων και στα νησιά του Β.Α. Αιγαίου, με κυριότερα τη Λέσβο, τη Χίο και τη Σάμο, οι οποίες δε σχετίζονται με άλλα φαινόμενα ούτε με νεφοκάλυψη. Αντίστοιχες περιόδους θερμικών ανωμαλιώνέχουμε τον Οκτώβριο του 2014 με 20 μέρες συνεχών ανωμαλιών στις ίδιες περιοχές, 7 ημέρες τον Ιούνιο του 2012 στη περιοχή της Χίου και 11 ημέρες (16/07-26/07) στη Χίο και στη Νίσυρο τον Ιούλιο του 2007. Τα πρώτα αποτελέσματα εφαρμογής της μεθόδου δείχνουν συσχετισμό των ανωμαλιών με ηφαιστειακή δραστηριότητα αλλά

και πιθανώς με την άνοδο και την κυκλοφορία του υδροθερμικού νερού μέσω ρηγμάτων.

ABSTRACT

The Aegean Sea consists of islands with strong geothermal activity due to the volcanism that exists in the Aegean Volcanic Arc (AVA). The Land Surface Temperature (LST) product of the Moderate Resolution Imaging Spectro-radiometer (MODIS) sensor is used for the first time herein, in order to capture and map the possible outbreak of volcanic/geothermal activity on the already known volcanic/geothermal fields. The innovation that applied in this Thesis is the application of the technique RST (Robust Satellite Technique), a statistical method for the elimination of the noise from the data and the signal amplification for its best detection and so for better quality's results. The data-sets cover a time-period of 12 years (2003-2014) and they regard to daily images. At first, the ALICE index is applied for the calculation of the anomalous TIR pixels with monthly and after with daily duration window. Subsequently, the RETIRA index is being used in order to eliminate the influence of climatic conditions. The indexes were applied in the GIS environment where new tools were developed through the Model Builder. The strongest thermal anomalies are detected in the islands of; Lesvos, Chios, Kos, Samos Ikaria, Nisyros and Santorini, where in the first 5 are of high frequency and duration. The main thermal anomalies are found from April to October while in the remaining months appear mainly false positive anomalies, due to the high cloud-coverage. In many cases, these anomalies don't seem to be related with phenomena like seismicity and forest fires. Characteristically, on October 2013 we have an anomalous time-period of 24 days (4/11-28/11) on the islands of Dodekanisa and on the N.E Aegean islands, with most notable the islands of Lesvos, Chios and Samos, which are not related with any other phenomenon or cloud-coverage. Moreover, thermal anomalies have been detected in October of 2014, for a time-period of 21 days, 7 days in June 2012 on Chios's area and 11 days (16/07-26/07) on Chios and Nisyros in 2007. Finally, the preliminary results of the applied method show a correlation of the revealed anomalies with the volcanic/geothermal activity and probably with the uplifting and circulation of the hydrothermal water through the radial and tectonic faults.

Table of Contents

Chapter 4: Results

Conclusions

ΠΡΟΛΟΓΟΣ

The main aim of this Thesis is the observation of the varieties in the geothermal activity on the already known geothermal/volcanic fields of the Greek East Aegean Sea and the Aegean Volcanic Arc by using Remote Sensing and MODIS-LST imagery. The indexes ALICE-RST and RETIRA-LST were implied for the first time for this purpose.

The most part of this study completed in the laboratory of Geophysics and Seismology on the Technical Institute of Crete in Chania, Greece and a part of it on the Remote Sensing and Earth Observation at the Satellite Data Analysis Laboratory (LADSAT) of Engineering School of University of Basilicata in Potenza. The duration was two years (October 2014 – August 2016).

The current thesis is organized in five chapters;

The first one refers to the geothermal fields and their connection with the Aegean volcanic arc, by providing general information for both of them, along with some historical events/eruptions and also with their situation today. It is also presented the chosen time-period and area of our data.

In the second chapter are being discussed the methods and technologies of monitoring the geothermal activity, giving an emphasis to MODIS-LST product.

Next, in the third chapter I describe the Robust Satellite Techniques and all the analysis that was carried out, from the creation of the historical data-sets to the ALICE-RST and after to RETIRA-LST applications.

Finally, in fourth chapter are the results of this Thesis in detail and at the end the conclusions.

INTRODUCTION

Greece is endowed with numerous thermal and mineral springs (Giono-Stavropoulou 1983; Sfetsos 1998) due to volcanism and its unstable geodynamic pattern (Zougias, Miliaresis, Seymour, 2010). The most important of them, like Nisyros and Milos islands belong on the Aegean Volcanic Arc (AVA) and around it. This is a fact since the volcanic activity is totally connected with the geothermal and hydrothermal activity. The active tectonics and the volcanic activity determined the high heat flow affecting the Hellenic area since Tertiary because of the collision between the European and African tectonic plates (Fytikas et al., 2005).

The existence of a geothermal field is related to volcanic activity and volcano-related phenomena such as calderas, thermal springs, and circulation of thermal waters. Identification of such thermal anomalies can be detected by Remote Sensing methods and verified by field measurements (Zougias, Miliaresis, Seymour, 2010).

Geothermal activity belongs to one of the natural phenomena that the last years presents a great scientific interest due to its connection with important natural hazards, such are the volcanic activity and the seismicity, and also with economic matters since it one of the renewable energy sources with the most beneficial factors, among others, in the production of electricity and heat. The main benefits by using this source are that the external factors, like weather and sun, do not affect the production of geothermal energy. For this reason it is characterized as a stable and reliable energy source. The geothermal systems belong to three main categories, based on reservoir fluid temperatures and these are; (i) with high enthalpy; (ii) with medium enthalpy; and (iii) with low enthalpy.

For all of the above we consider very important the monitoring of the geothermal and volcanic fields. There are two approaches for the monitoring; the first with ground-based measurements and the second by using Remote Sensing Techniques and satellite images. For the better result, a combination of the two is needed. As for the second approach, modern operational space-borne sensors with spectral sensitivity in the thermal infrared spectrum allow monitoring of the Earth's thermal field at a moderate spatial resolution (Lillelsand and Kiefer 1987). A variety of sensors/satellites that are appropriate for the monitoring of the geothermal fields is

available, along with a numerous products that each one includes. According to the chosen analysis and its final purpose, such as the land surface temperature, the extracted gasses measurements, the ground deformation etc. we choose one of the available sensors and products.

The Land Surface Temperature (LST) is a key parameter in the physics of land surface processes from local through global scale (Andersonet al., 2008; Brunsell & Gillies, 2003; Karnieli et al., 2010, Kustes & Anderson, 2009, Zhang t al., 2008). Satellite remote sensing enables estimations of the LST over wide areas (where there is a strong spatial heterogeneity in land surface characteristics, such as vegetation, topography and soil physical properties; Li et al., 2013), with a different temporal coverage. The requirement of land surface temperature (LST) inversion estimating accurately in geothermal exploration makes the remote sensing of LST a prevailing topic (Li, Lv, Wen, 2012). In particular, the LST may be retrieved analyzing both infrared and microwave satellite observations (Sun et al., 2006).

A variety of studies has been done in the monitoring of the geothermal fields by using the LST product. A probable regional geothermal field reconnaissance has been successfully carried out in the Aegean region from Zougias, Miliaresis and Seymour in 2010 using multi-temporal night MODIS-LST imagery. In another research multi-temporal LST imagery assisted geophysical interpretation in Afar Depression (Ethiopia) and allowed the identification of the major geothermal field (Miliaresis et al., 2009). In the Tengchong volcanic-geothermal area of southwest China (Xiong, Chen, Huang, 2016) three out of eight in total geothermal fields were identified by using remote sensing technique and LST imagery, along with information of geologic structure and hydrothermally altered rocks. Two possible geothermal fields are found to be located under the zone of Tangshan in 2012 by using thermal infrared and LST maps. Some investigations in field survey reveal a close correlation between the geothermal anomalies and the distribution of hot springs. The feature of geothermal anomalies also indicates that the geothermal anomaly areas in Tangshan are subjected to the development of fault structure (Li, Lv, Wen, 2012).

The ALICE (Absolute Local Index of Change of the Environment) index, which belongs to the statistical approach named Robust Satellite Techniques (RST), has been proposed in order to detect the environmental anomalies. For the detection of the anomalous pixels we need to have time-series of data of satellite TIR images. In this way we can build homogenous maps that include for its pixel the "normality" value, and then by comparing each single map that we have with them we will be able to observe the anomalous pixel.

Especially in the TIR anomalies the weather conditions still affect the results even after the application of the ALICE-RST application, so a more specialized index has been using for their deletion with the name RETIRA. It has to be mentioned here that it is the **first** time that the RETIRA–RST index is been using for the detection of the TIR anomalies in geothermal activity.

A time period of 12 years (2003-2014) has been chosen for the area of the East Aegean in Greece, bound by latitudes 25°-28° N and longitudes 35°-$39o$ E, where occur some of the most significant Greek geothermal fields on the AVA and out of it. We considered MODIS-LST as the appropriate product for three reasons; (i) because of the data's availability, which was free from NASA's [REVERB](#) website, (ii) because the spatial resolution is 1km, so we could have a valid information for our area which is full of islands and (iii) because it could provide us daily homogenous data (at the same hour, area etc.). Both of the ALICE and RETIRA indexes were applied for the analysis, having as a result the comparison of them for this type of analysis. The main platform that was used is ArcGIS and a number of new toolboxes were created for the pre-processing of the images and for the calculation of the indexes. After the application of the indexes we tried to observe which of the anomalies are true or false alarms, by looking also at the earthquakes that occurred in each area around the anomalies for a specific period of time. Information of previous ground-based measurements from other studies are including for the best final result.

Chapter 1

Greek geothermal fields and the connection with the Aegean Volcanic Arc

1.1.: Introduction to geothermal fields

With the terms "geothermal", we refer to any system that transfers heat from within the Earth to its surface (Heasley and Foley, 2009). A geothermal system includes a heat source (e.g. a magmatic intrusion at shallow depths) a reservoir (i.e. hot permeable rocks overlain by a cover of impermeable rocks) and a geothermal fluid (i.e. generally meteoric water in the liquid or vapor phase depending on its temperature and pressure). Once the geothermal fluid containing chemicals and gases is heated (e.g. by warm rocks in the presence of a normal geothermal gradient when water reach high depths), it may escape from reservoir driven by pressure or density along faults and fissures producing springs, geyser or fumaroles (e.g. Heasley and Foley, 2009) or it may extracted from boreholes. A colder meteoric water coming from the margin of the system (i.e. a region which may be located up to tens of kilometers from the discharge site) replaces the discharged fluid.

Hence, the geothermal (hydrothermal) activity occur with the rise of hot fluids through permeable rocks in areas where the geothermal gradient (i.e. the rate of increasing temperature with depth) is even more than ten times the average value (2.5-3°C/100 m) (International Geothermal Association, 2016).
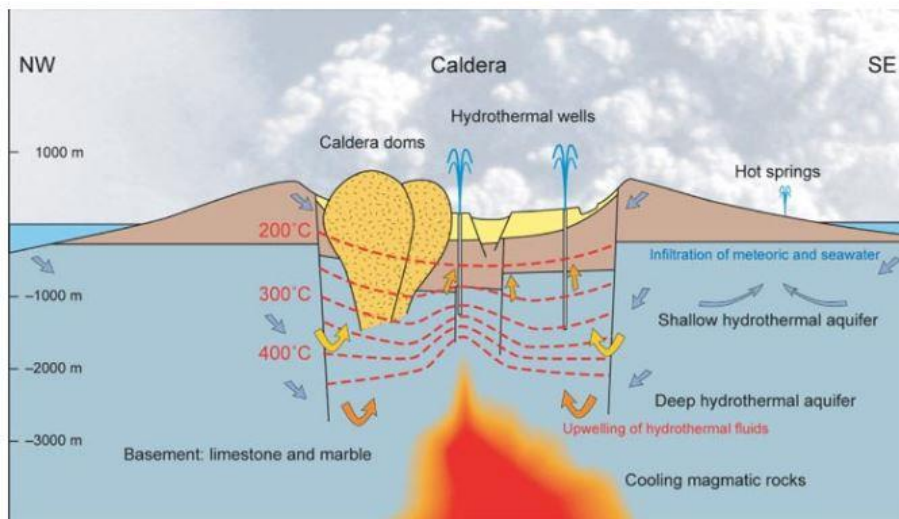
Fig.1: The circle of a geothermal system
Source: http://www.aegean-energy.gr/en/pdf/nisyros-project.pdf

According to classification proposed by Muffler and Cataldi (1978), geothermal fields may be grouped in three main categories based on reservoir fluid temperatures:

- High enthalpy (i.e. over 150°C);
- Medium enthalpy (i.e. 90°C – 150°C);

- Low enthalpy (i.e. less than 90°C).

Geothermal fields of high enthalpy mostly occur at plate boundaries although they also affect continental rifts and hot spot environments. They show a heat flux three or four times higher than the normal one with temperatures reaching also 400°C (Dickson and Fanelli, 2004). They are water or vapors dominated and include fumaroles, steam vents, mud pools, and highly altered ground (Saemundsson, 2009). The medium and low geothermal fields show a heat flux lower than high enthalpy geothermal systems. The low enthalpy systems are affected by regional geothermal gradient, permeability of the rock and depth of water circulation (Saemundsson, 2009). It is worth noting that a number of authors classified the geothermal fields using different temperature ranges than those reported above (e.g. Benderitter and Cormy, 1990; Haenel et al., 1988). To overcome ambiguities in the temperature/enthalpy classification, an alternative categorization of geothermal resources in terms of exergy (i.e. the energy that is available to be used) was proposed by Lee (2001) developing a specific index aiming at defining low, medium and high quality classes.

1.1.1.: Geothermal fields in Greece

The geothermal exploration that was performed in Greece in the seventies at Institute of Geological and Mineral Exploration (IGME) by means of geological mapping, geochemical and geophysical surveys, studies of heat flow (fig. 3) and recent volcanism, revealed the presence of geothermal fields in several areas of Greece (IGME, 1983; Koroneos and Fytikas, 1999; Mendrinos et al., 2010). The most important geothermal regions of high enthalpy in the country are the Aegean Volcanic Arc (AVA) and the islands of Milos and Nisyros (Baba and Bundschuh, 2014). In these regions, some field observations have shown that temperatures of geothermal fluids may exceed 300°C (e.g. Chiotis and Vrellis, 1995). Fytikas and Kolios (Fytikas & Kolios, 1979) constructed a heat flow map of Greece (fig. 2) using these data (Jongsma, 1974), (Ericson et al, 1976) and (Hsu et al, 1975) as well as additional data of their own (Fytikas & Kolios, 1979). In places where the available heat flow data were not adequate, measurements of surface hydrothermal phenomena (thermal springs, fumaroles and hot grounds) and thermal measurements in drill holes done for

geothermal investigations were taken into consideration by Fytikas and Kolios (Fytikas & Kolios, 1979) in order to characterize the heat flow pattern and complete the heat flow map. These phenomena in the major volcanic centers of the Aegean Sea (Greece), i.e., Sousaki, Methana, Milos, Santorini (Thira), Kos and Nisyros, show high temperature gradient and high heat flow (Fytikas & Kolios, 1979). The active tectonics and the volcanic activity determined the high heat flow affecting the Hellenic area since Tertiary because of the collision between the European and African tectonic plates (Fytikas et al., 2005). Geo-thermal fields of medium-low enthalpy, that are mostly associated with grabens and post-orogenic sedimentary basins (Fytikas and Arvanitis, 2009), characterize the rest of the AVA and the Northern Greece (Thrace, Macedonia) while low enthalpy geothermal activity exists almost in all over the country. The low enthalpy systems are associated to a deep-water circulation with temperatures less than 100 ºC, most of which are located in basins in Northern Greece and in many Aegean islands (Andritsos et al., 2015). Indeed, since a geodynamical, very active area characterizes most of the country, Greece is rich in geothermal waters (Fytikas, et al., 2000) (Papadakis et al., 2016).
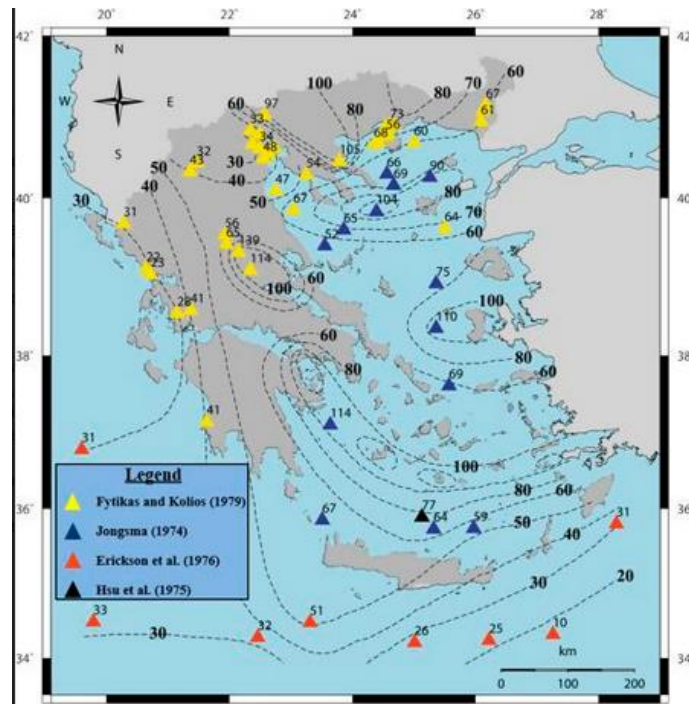
Fig.2: Heat flow map of Greece by Fytikas and Kolios [8]. The heat flow values are presented in mW m−2.

According to the heat flow map (Fig. 2), low heat flow values are observed along the HSZ and in the western part of mainland Greece, whereas high heat flow values are concentrated along the active volcanic arc, in the central Aegean Sea (around the island of Chios) and along the NAT. In the volcanic arc, high heat flow values range between 80 and 120 mW m^{-2} (Papadakis et al., 2016). Relatively high heat flow values are observed in central and eastern Macedonia and in the area between the north-eastern part of central Greece and the southern margin of the Thessaly basin. In the following, the main areas of Greece that are characterized by the presence of geothermal fields (see Fig. 1) are described in detail.
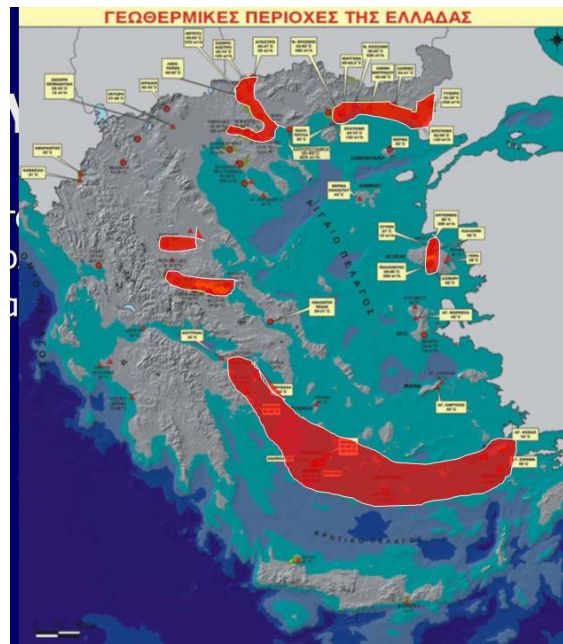
Fig. 3: Areas of geothermal interest in Greece and the Aegean Volacnic Arc.
Πηγή: M. Fytikas, (2014), Γεωθερμία, η μεγάλη αγνοούμενη ΑΠΕ στην Ελλάδα

Nisyros and Kos Islands: They are located in the Complex of Dodekanisa islands and belong to the Aegean Volcanic Arc, with the small island Nisyros representing the second most active area in terms of geothermal resources. The islands of Nisyros, Yalli, Petra, Pergousa, Pachia and Strogili did not exist before the historical eruption of Kos Island occurred 160.000 years ago.

In both islands, we can find volcanic rocks and sediments, and thermal waters of all types of enthalpy and thermal spring used by public. Those springs are well known since the ancient years, with important Greek personalities, like Hippocrates, and Roman ones which spoken about them.

Kos and Nisyros were covered from magma and volcanic ash when the above mentioned huge eruption occurred. Nisyros is a stratovolcano known for its intense hydrothermal activity. The geothermal fields on this island can reach temperatures above 300°C. The total dissolved solids are up to 10 to 30 gr/lt and the concentration of hydrogen sulfide is at high level. The low enthalpy geothermal fluids that emanating from reservoirs at depth 30-120m, show temperatures between 25-95°C (Koroneos and Fytikas, 1999).

Lesvos Island: It belongs to the complex of "Islands of the North-Eastern Aegean".
third bigger Greek island and it is well known for the thermal springs and the last months for the refugees who come there mainly from the Middle East.

Fig. 4: The petrified forest of Lesbos island.
Πηγή: http://wikimapia.org /9399561/el/To-
Απολιθωμένο-δάσος-της-Λέσβου

Mostly medium but also some high enthalpy geothermal fields along with hot springs can be found at Lesvos due to tensional tectonism on the area, which is a result of the sinking of the African plate, under the Eurasian plate. The places with the greatest enthalpy are: *(a)* Argenos, *(b)* Stipsi and *(c)* Polichnitos. In the area of Vatousa Sigriou there is a caldera with 100 m^2 range and an incredible beautiful petrified forest. We should mention that the Petrified Forest is one of the two largest Petrified Forest in the world with a covering area of 150 km^2 (Fig. 4). It represents a World Heritage of UNESCO. Moreover, Lesvos offers the hottest thermal bath in whole Europe with 88°C (whose system is shown in Fig. 4). The Lesvos's geothermal energy is currently exploited for the warming of greenhouses with thermal springs that are used for medical baths.

Santorini Island: Santorini is a volcanic Island group at the central south end of the Cyclades in the Aegean Sea of Greece. People around the world know it for the volcano that contains, which made one of the most important historical explosions on

the world's history around the 1600 BC, for the incredible and characteristic Greek-islandic architecture with the white buildings and the blue/green windows and also for the unique view of the sunset. This island belongs to the AVA and represents the most quiescent volcano in Greece. The last eruption took place in 1950, with some seismic crises, magma uplift, soil deformation and other volcanic-related phenomena that were recorded since then.

The Santorini Island Complex has five areas: Thira, Thirasia, Palea Kameni, Nea Kameni and Aspronisi. The last three include the caldera rim of the island. Around and very close to Santorini there is the volcanic islands "Christiana" and the Kolumbo submarine volcano.

According to «M. Fytikas, (2014), Γεωθερμία, η μεγάλη αγνοούμενη ΑΠΕ στην Ελλάδα», Thira (Santorini) is characterized as an island of medium enthalpy from 110°C to 150°C with the geothermal activity occurring at depths of 800-1000 m.

Chios Island: Chios is also a part of the "Islands of the North-Eastern Aegean", under the island of Lesbos. Volcanic centers and thermal waters exist in the southern part of the island (i.e. in the area of Nenita) as well as in the northern part (i.e. in the areas of Aghia Markela and Aghiasmata). The geothermal liquid in the northern side is a mixture of a local groundwater and arc-type magmatic water that did not exchange oxygen isotopes, or a mixture constituted by local groundwater and seawater that experienced a significant isotope exchange. Based on chemical and isotopic geo-thermometer, it was speculated the existence of a deep geothermal reservoir of high enthalpy around 220°C in the northern part of the island and of one of low enthalpy around 80°C for Nenita in the southern part (E. Dotsika, I. Leontiadis, D. Poutoukis, R. Cioni, B. Raco, 2006).

1.1.2 Importance of monitoring geo-thermal field variations

The monitoring of geothermal fields is very important especially in sites of intense geothermal emissions. In fact, the analysis of geothermal resources allow us to assess their possible usage as a renewable energy source (e.g. heating of houses/greenhouses, producing electricity), as thermal springs for the public (e.g. for medical reasons), and most important as indicator of the status of volcanic activity in high-risk areas. Geothermal fields can change as a result of local or distant evets that after the water

source or flow path the heat source, thermal characteristics along the subsurface flow path, and/or the fractured rock that the waters are flowing through (Heasler & Foley, 2009). In fact, to map the geothermally heated areas is important for recognizing future anomalous hydrothermal and or volcanic features (Vaughan et al., 2013).

Geothermal fields of high enthalpy that are generally associated to areas of young volcanism characterize regions located along the tectonic plate boundaries. The relation of geothermal fluids with regions of induced seismicity and with the active volcanism is described in the next section.

1.1.2.1 Induced Seismicity

The exploitation of geothermal resources during production and injection operations (fluids injection helps to maintain reservoir pressures and flow rates at production levels), may induce low magnitude seismic events (Antayhua-Vera et al. 2015). Hydrothermal (geothermal) systems can provide early evidence of earthquakes (Fournier et al., 1991). According to Hubbert and Rubey (1959), an increase in pore pressure because of water injection would in fact reduce the effective strength of rock. Micro-earthquakes (usually having a Richter magnitude of 2-3) generated by fluid injection at geothermal fields generally do not represent a risk for the geothermal power plants and local population. However, since geothermal operations are generally performed in active tectonic areas is generally difficult to distinguish between geothermal-induced and natural seismic events (Geothermal Energy Association, 2016). For instance, the Geysers Geothermal Field (GGF) represents one of most important geothermal resources in the world. In this geothermal area, seismicity may occur not only for changes in fluid pressure but also because of other factors such as stress changes due to tectonic, thermal and for poro-elastic forces (Cladouhos et al., 2010). It should be stressed that although injected water may improve the quality of produced steam from a chemical view point, it could migrate along fractures reaching production wells, determining a degradation of the geothermal production. A complete description of the impact of fluid injection on induced seismicity that is beyond the aim of this thesis can be found in some literature works (e.g. Maier and Peterson, 2007).

Changes in permeability can occur as minerals precipitate along fractures and fill pore space and as earthquakes open or close fractures.

1.1.2.2. Volcanic activity

Volcanic hazard forecasting is becoming more quantitative and is based on an understanding of volcanic system processes (Sparks et al., 2003). In a magmatic hydrothermal system, the magma heats rocks that then deep circulating waters (Heasler & Foley, 2009). In fact the highest's temperature's geothermal systems are found in regions with active or geologically young volcanoes.

Changes from active to inactive and back again may be typical of hydrothermal systems (Moore, 2007), so by monitoring geothermal (hydrothermal) systems may help to determine whether the systems are heating up, cooling down, or remaining the same (Heasler & Foley, 2009), as long as providing early evidence of moving magma, by the change in the heat source. Groundwater level changes have been also very important in recognizing unrest periods and eruptions, by using modern deformation monitoring technology. Increases in spring flows have been also noted prior to eruptions (Omori 1914; Koto 1916).

It is a fact that there is currently no numeric summary of overall intensity of the various volcanic unrest phenomena that can be used to compare the intensity or frequency of unrest over time or which can be used to communicate this information to non-scientists (Potter, Scott, Jolly, Neall & Johnston, 2015). For this reason a worksheet of a Volcanic Unrest Index (VUI) was created, based on a scale from 0 to 4 of observed rest of unrest (table 1).

Preliminary of a Yellowstone geyser suggests that it may have had periods of activity that were separated by perhaps thousands of years of quiescence (Foley et al., 2006).

Another example is for the Norris Geyser Basin where calibrated temperature maps provide baseline information about heat flow and the changes in it. The scientists after can create heat flux maps to provide a quantitative estimate of heat flow for the entire Norris hydrothermal area annually or over multiple years (Heasler & Foley, 2009).

Sudden groundwater level drops have been noted on a number of occasions as a result of inflation and draining of reservoirs at Kilauea in Hawaii in 2001 (Hurwitz and Johnston, 2003) and in Mt. Usun in Japan prior to an eruption in 2000 (Shibata et al., 2008).

Volcano: ___ Area used: ___ Date applied: ___ Real-time / Past episode Time window: ___	**Volcanic Unrest Index (VUI) Worksheet**					VUI = ___
	0 No unrest	**1** Negligible unrest	**2** Minor unrest	**3** Moderate unrest	**4** Heightened unrest	
Local Earthquakes — Duration of earthquake swarm (all EQ types)	No earthquake swarm	Short (≤ ___ time unit)	Short to moderate (≤ ___ time unit)	Moderate to long (≤ ___ time unit)	Long (> ___ time unit)	Use only the highest of these 2 scores
Location of earthquakes (all EQ types)	No locatable EQs or generally deep hypocentres (> ___ km)	Moderate depth (___ ≤ ___ km), or shallow depth (≤ ___ km) and distant from likely vent (≤ ___ km)			Shallow (≤ ___ km) and close to vent (≤ ___ km), or unlocatable tremor	
Maximum rate of volcano-tectonic (VT) earthquakes	No VTs or low rate (0 ≤ ___) of low magnitude (≤M ___) EQs per time unit	Moderate rate (≤ ___) of low magnitude (≤M ___), or low rate (1 ≤ ___) of high magnitude (>M ___) EQs per time unit	High rate (> ___) of low magnitude (≤M ___), or moderate rate (≤ ___) of high magnitude (>M ___) EQs per time unit	High rate (> ___) of high magnitude (>M ___) EQs per time unit	Rapid acceleration in rate, may include sudden decrease in rate	
Tremor, low-frequency and hybrid earthquakes	None		Weak tremor (≤ ___ units) or low rate of LF or hybrid EQs (1 ≤ ___ per time unit)	Moderate tremor (≤ ___ units) or high rate of LF or hybrid EQs (> ___ per time unit)	Strong tremor (> ___ units)	
Local Deformation — Maximum rate of local deformation	No deformation	Low rate of deformation (≤ ___ units per time unit)	Moderate rate of deformation (≤ ___ units per time unit)	High rate of deformation (> ___ units per time unit)	Rapid acceleration in rate of deformation, or sudden decrease in rate	
Location of deformation source (e.g., through modelling)	No deformation	Slowly deflating source or local tectonic fault movement	Deep inflating source (> ___ km)	Inflating source at a moderate depth (≤ ___ km)	Shallow (≤ ___ km) inflating source or migration towards the surface	
Groundwater levels and spring flows	Levels and spring flows reflect that of surrounding areas	Low levels and spring flows. May include wells or spring-fed ponds drying, or streams ceasing to flow		High levels or spring flows. May include hot or cold water spouting (not geysers), or high stream-flow/lahars without corresponding rainfall or lake contribution		
Geothermal systems and degassing — Surface temperature, heatflow, and manifestations	Ambient temperatures, no above-ambient heatflow, no active surface manifestations	Above ambient temperature, heatflow or activity at surface manifestations	Heatflow or temperatures near or at boiling conditions, or moderate activity at surface manifestations	Geothermal system hotter than boiling conditions, may include hydrothermal eruptions	High heatflow, temperatures or activity, may include phreatic eruptions	
Gas flux	Low levels of gas flux (≤ ___ t/day of CO₂ and ≤ ___ t/day of acid gases)	Moderate levels of gas flux (___ ≤ ___ t/day of CO₂ or ≤ ___ t/day of acid gases). Effects may include gas-induced vegetation kill or effect on animal life			High levels or acceleration of gas flux (> ___ t/day of CO₂ or > ___ t/day of acid gases), or a sudden decrease	
Gas and fluid composition	Meteorological signature	Hydrothermal signature	Mixed to magmatic signature	Magmatic signature		

Table 1: The Volcanic Unrest Index (VUI) framework and worksheet
Paper source: Introducing the Volcanic Unrest Index (VUI): a tool to quantify and communicate the intensity of volcanic unrest.

1.2.2: The Aegean Volcanic Arc today

The Aegean Volcanic Arc is a half – sleeping volcanic arc, with Santorini and Nisyros representing the most "active" volcanic islands. In spite of the current volcanic status (i.e. 1 out of 5) which the same of other Greek volcanoes these islands are well monitored by a ground-based surveillance system. Thermal, chemical and hot fluid's composition monitoring are carrying out mainly by the Institute of Study and Monitoring of Santorini Volcano (ISMOSAV), which is a prestigious Greek non-profit organization founded in 1995. Moreover, seismic monitoring is performed by a local network of seismic networks installed by the Geodynamic Institute of the National Observatory of Athens in co-operation with the Laboratories of Geophysics of the University of Thessaloniki and Athens (Mario-Cesar Suarez Arriaga, Fernando Samaniego V., Joshua Mendez Harper, 2010). Regarding the Nisyros Island, the volcano entered in a phase of quiescence (i.e. status 1 out of 5) after the seismic crisis of 1993. Several recent studies have been performed to investigate this volcanic

complex showing some interesting results. They include the discovery of several submarine volcanic centers and massive underwater volcanoclastic deposits along with the identification of soil deformation and gas emissions with temperatures of fumaroles increasing up to 103°C during 2004 (Nomikou et al., 2013).

Concerning the Santorini's volcanic complex, the most recent explosion took place in 1950. It was the last from the Greek volcanoes. Currently, the magmatic activity is almost stable in spite of the occurrence of some seismic unrest periods. Specifically, from January 2011 to February 2012 an important increase of the seismic activity was recorded along with a significant deformation of the ground (of about 10 cm) that was revealed by satellite measurements and interpreted as the inflation of a magmatic source (e.g. Newmann et al., 2012). Moreover, other studies revealed changes in the water temperature and elevated gas emissions. Finally, volcanological bulletins reported the occurrence of two minor seismic crisis during 2015 and 2016.

1.2.1 Historical eruptions

The Greek volcanoes are not as active today as other volcanoes, but they have a truly important history for which they are well known.

A number of eruptive events characterized the volcanoes belonging to the Aegean Volcanic Arc. They include the islands of Nisiros, Santorini, Milos, Methana and Soysaki. The eruptive episodes of first two volcanic areas are summarized respectively in Table 2.

Concerning the Milos, Methana and Soysaki since these volcanic regions are outside the area of interest for this work their historical eruptions are not discussed here.

Nisyros (Fig. 7) is a very young "island" that age only 165.000 years above the sea level. At that time, an enormous explosion took part on the volcano of Kos Island where 240 billion tons of melting rock affected the island, with volcanic ashes reaching also the Turkish coast and the islands of Kalymnos and Tilo Islands. In more detail, more than 100 km^3 of pyroclastic products were emitted destroying an area of about 3000 km^2 (Keller et al., 1990). Nisyros began its evolution with the submarine build up of basaltic-andesitic pillow lavas and hyalo-clastites and eventually emerged above sea level allowing the development of a subaerial edifice (Kinvig, Winson &

Gottsman, 2010). However, the current morphology of volcano derives from a series of following eruptive events.

The Minoan plinian eruption of Santorini's volcanic complex and Kolumbos submarine volcano took place around 1645 B.C. in the Late Bronze Age. This eruption producing a column height estimated around 36-39 km (Pyle, 1990) was considered as the main reason of collapse of the Minoan civilization, although since Knossos was 60 m above the sea level the tsunami did not reach it. In addition, this eruption was one of the most catastrophic recorded in the human's world history, with the estimated Volcanic Explosivity Index (VEI= 6) putting it in the second place along with the Krakatau eruption in 1883 and just under the Tambora volcanic explosion

(VEI=7) of 1815. The Santorini eruption affected even the major areas in Western Mediterranean region. Moreover, small tsunamis were generated with the largest one that was associated to Kolumbos submarine volcano where because of eruption the magma chamber collapsed and the existing caldera became larger. This eruption had a huge impact both on human life and on environment and affected the climate changes at a global scale.

SANTORINI		
Year	**Events**	**Comments**
1950: 10/01/1950-2/2/1950	Small effusive activity preceded by phreatic explosions.	
1941	Eruption. Slightly explosive activity	Formation of several lava domes
1925-1928: 11/08/1925-17/03/1928	Eruption. Moderate effusive and explosion activity. Lava flows, lava mountains and ash-falls	Growth of Nea Kameni
1866-1870: 04/02/1866-15/10/1870	Eruption. Moderate effusive and minor explosive activity. Lava flows, lava fountains and ash -falls	Mikri and Nea Kameni unite.
1707-1711: 23/05/1707-Sept/1711	Eruption. Strong and effusive activity.	Formation of Nea Kameni. Lowering of the coastline of
NISYROS	Ash-fall and gas explosions.	Thera and Mikri Kameni
1650: 27/09/1650	Eruption of Kolumbo submarine volcano Ash and pumice fall and toxic gasses	Generation of a strong tsunami
1570	Eruption	Formation of Mikri Kameni
726 A.D.	Strong explosive - probably sub-plinian eruption	Creating the black blocky lava dome of Aghios Nikolaos
46 A.D.	Eruption	Appearance of a new island
197 B.C.	Eruption	Appearance of Palea Kameni
1613 +- 13 B.C.	Minoan Eruption	

Year	Crater	Events	Commens
1881-1887	Micros Polyvotis	Hydro-thermic explotions	
1500-		Hydrothermal explosions	
1,000-2,000 B.C.	Stefanos	Hydro-thermic explosions	
5,000-10,000 B.C.	Kaminakia craters	Hydro-thermic eruptions	Creation of lava domes in Argos and Pachia ammos
15,000-10,000 B.C.		Building of post-calderic volcano domes	
15,000 B.C.	Central caldera of Nisyros	Effusive eruption	Creation of the "Upper Pumice"
25,000 B.C.	Central caldera of Nisyros	Effusive eruption	Creation of the "Lower Pumice"
40,000-30,000 B.C.		Effusive eruptions	
150,000-170,000 B.C.		Violent explotions and low volcanic activity	Transformation into a stratovolcano
150,000 B.C.		Fist submarine eruptions	Creation of the onshore cone

Table 2: Eruptive periods

Fig. 6: Image of the last eruption in Santorini in 1950
Source: http://www.greece-is.com/born-of-fire/

1.3.: Testing Area and period
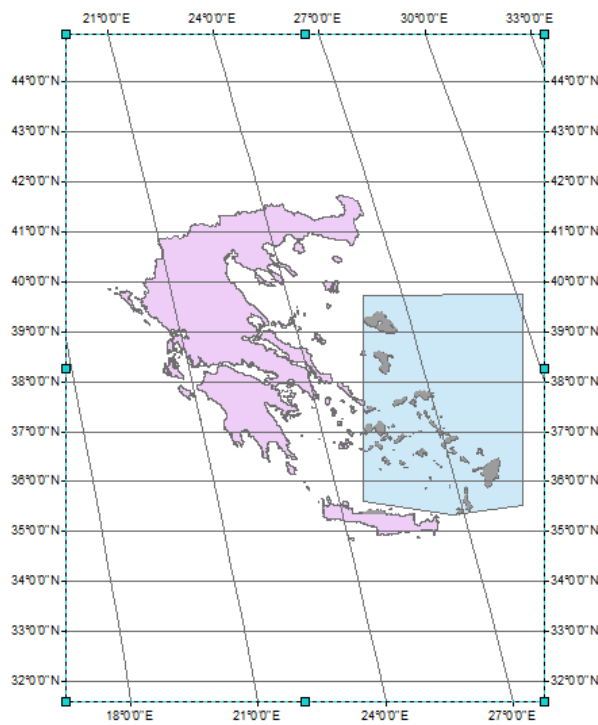
Fig.7: The map of Greece with the selected area
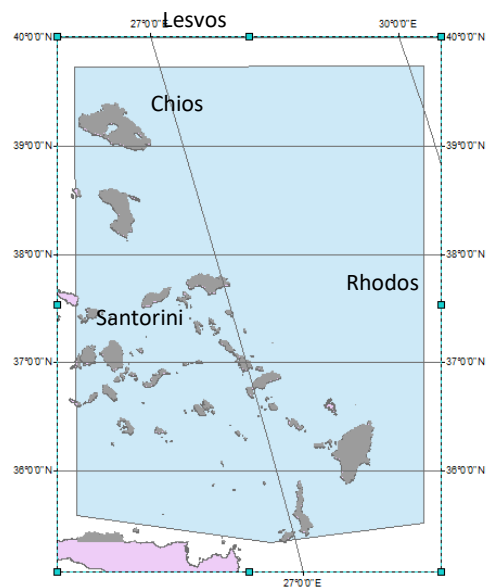
Fig.8: The testing area.

The testing area (fig.8) corresponds to Middle – Eastern Aegean bounded. In this area are included the biggest and most active part of the AVA (Aegean Volcanic Arc) and the places –islands- with the greatest enthalpies of geothermal activity in Greece. Since the islands have a small land-coverage, we didn't want the rest of the country to be participated inside our images, because it would probably affect our results in the calculation of the reference fields.

Our images are daily from January 2003 to December 2014. This 12-year period was used for both the reference fields and the analysis of the data. During this time we had a seismic crisis around Santorini's volcano from January 2011 until March 2012 that worried the scientists for an activation of the volcano.

CHAPTER 2

REMOTE SENSING: METHODS AND TECHNIQUES

2.1 Remote Sensing Techniques

According to Gupta, Remote Sensing (RS) can be defined as the capability of obtaining information about an object without being in physical contact with it (Gupta, 1991), typically from aircraft or satellites. In order to collect data the remote sensors detect the energy that is reflected or emitted from the Earth's surface. The transmission of the information from the object/event to the sensor happens through the electromagnetic radiation. Generally applies that whatever natural/artificial body emits and/or reflects at different wavelength ranges of the electromagnetic spectrum is depending on its own physical/chemical features (Tournaviti, 2013). So that, provided that devices suitable for detecting electromagnetic radiation at different wavelength are used, it will be possible to recognize the body that produced them (Rees, 1990). The two main categories of remote sensors are; (a) passive sensors, where are often referred to as electro-optical or simply optical, acquire the reflected electromagnetic waves of the sunlight and/or the emitted infrared radiation by objects on the ground and (b) the active sensors, where are commonly referred to as synthetic aperture radar (SAR) or simply radar, provide their own energy to illuminate an area of interest and measure the reflected signal.
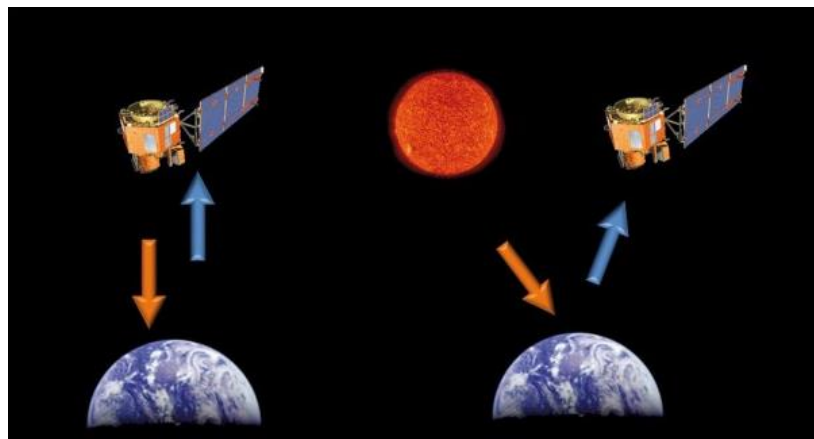
Fig. 9: An active sensor (on the left) and a passive sensor (on the right)Source:
http://eijournal.com/print/articles/exploring-the-benefits-of-active-vs-passive-spaceborne-systems

Some of the main advantages of using RS are; (a) synoptic overview which refers to large areas that are difficult accessible from the ground, (b) the high sampling

frequency rate, which depends on each platform/sensor and refers to the homogenous data and (c) the multi-disciplinary application, where one platform includes different sensors providing data in different regions of the electromagnetic spectrum for the same area.

2.1.1 The electromagnetic spectrum

The electromagnetic spectrum is a continuum of energy from shortwave high frequency cosmic waves to longer wavelength low frequency radio waves. A consequence of atmospheric absorption is that certain radiation at specific wavelength in the electromagnetic spectrum are strongly absorbed and effectively blocked. According to the wave theory the electromagnetic waves (fig. 10) consist of periodic oscillations of electrical and magnetic fields originally generated by charged particles, and can therefore travel through a vacuum.
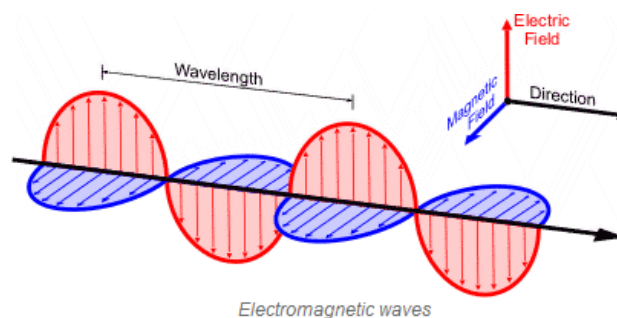
Fig. 10: Electromagnetic waves

Source: http://www.srh.noaa.gov/jetstream/remote/remote_intro.html

Wavelength and frequency are related by the following formula:

$$c = \nu\lambda$$

Where c is the speed light (2.99793x108 m/s), Therefore, the two are inversely related to each other: the shorter (longer) the wavelength, the higher (lower) the frequency.

There are the several regions of the electromagnetic spectrum:

- Gamma rays – Less than 0.01nm
- X-rays – 0.01- 10nm
- Ultraviolet (UV) – 10 nm- 400nm
- Visible - 390-750nm

- Infrared – 750nm – 1mm
- Microwave – 1mm- 1 meter
- Radio waves – 1mm – 1km

The light which our eyes (sensors) can detect is part of the visible spectrum (fig.11). The visible spectrum covers a wavelength from 0.4μm to 0.7μm and it divides in three primary areas –colors- of the spectrum. The blue is from 0.4μm to 0.5μm, the green from 0.5μm to 0.592μm and the red from 0.592μm to 0.7μm. In RS the sensors are able to "see" and recognize the electromagnetic radiation beyond the visible region, according to the research of interest, and by extracting an image in gray-scale makes us able to read it too. For example, the region of the infrared is one hundred times wider than the visible and it is divided in two categories; (i) the reflected IR and (ii) the emitted or thermal IR. The reflected IR is used in RS in similar way as the visible wavelengths and the thermal IR is slightly different, as this energy is essentially the radiation that is emitted from the Earth's surface in the form of heat.
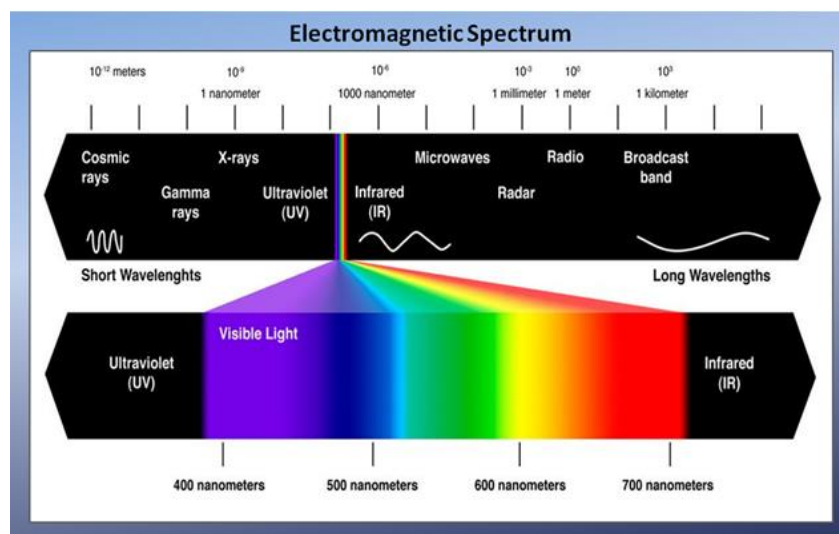
Fig. 11: Electromagnetic Spectrum and the visible region
Source: http://www.skepticalartist.com/2013/06/25/claude-monet-and-ultraviolet-light-did-the-master-impressionist-painter-have-uv-supervision/

2.2.2 Remote sensing parameters and characteristics

Remote sensing satellites are often launched into special orbits such that the satellite repeats its ground track after a fixed time interval. The two main orbits that are used are; (i) the sun-synchronous orbit and (i) the geo-synchronous orbit.

A Sun-synchronous orbit (fig. 12) is a geocentric orbit which combines altitude and inclination in such a way that an object in this orbit has a nodal regression rate which is equals to Earth's orbital rotation speed around the Sun. The object in this orbit constantly is illuminated by the Sun. This orbit is designed in such way that the satellite always crosses a given latitude on the 'day' side of the Earth at the same time of day. This has the benefit that the neighboring images can be easier stitched together since they will have the same lighting and the same direction of shadows and the benefit with this orbit the satellite is always overhead to the time that it is considered the best for imaging for the latitudes of greatest interest. Another great benefit is the much better spatial resolution of the polar-orbit satellites than the geostationary ones. A Sun-synchronous orbit has a particular inclination depending on the altitude of the satellite. Typical sun-synchronous orbits are about 600–800 km in altitude, with periods in the 96–100 minute range, and inclinations of around 98° and the lower the altitude, the closer the orbit is to the north-south direction.

Characteristics of polar and near polar orbits:

- full polar orbit inclined 90 to equator
- typically few degrees off (larger than 90)
- orbital period ,T ,typically 90 to 110 min
- near circular orbit between 300 km and 1000 km (Low Earth Orbit)
- typically higher spatial resolution than geostationary
- rotation of Earth under satellite allows (potentially) total coverage

Main sun-synchronous satellites are the MetOp (A & B), the NOAA (17, 18 & 19), the Terra and Aqua.
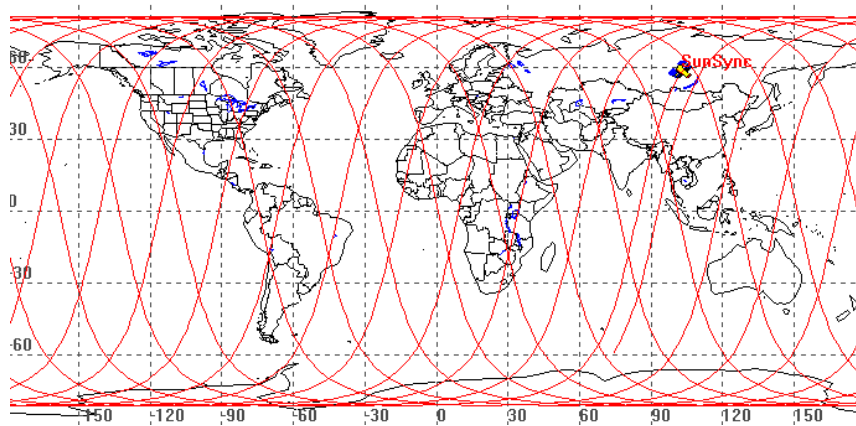
Fig. 12: A sun-synchronous orbit

Source: http://ccar.colorado.edu/asen5050/projects/projects_2000/redlin/

In the geostationary satellites the orbits are at the same speed that the Earth is turning, thus the satellite seems to stay in place over a single longitude, though it may drift north to south. A geosynchronous orbit (fig. 13) is circular and located in the equator and it is called geostationary orbit with an orbital eccentricity of zero.

Unlike the sun-synchronous satellites, the greatest benefit of a satellite in geosynchronous orbit is that it is able to see one spot of the planet almost all of the time. In this way we can monitor events and phenomena, with their variations, that took place during the whole day or more. At time there are 402 geostationary satellites according to Satellite Signals. It has typically low spatial resolution (lower than the sun-synchronous orbit) due to high altitude. Some of the main geostationary satellites are the GMS, the INSTAT, the GOES (E & W), the METEOSAT etc.
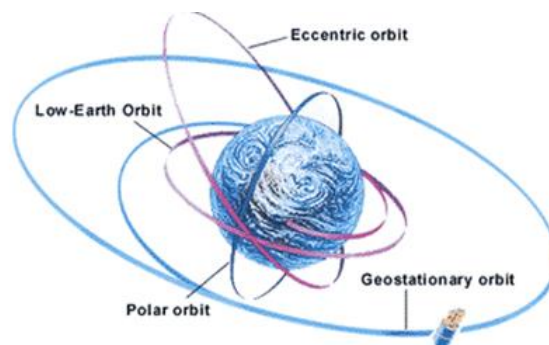
Fig. 13: Geostationary orbit

Source: http://poormansfriend.blogspot.gr/2015/11/geostationary-orbit-geosynchronous-orbit-satellite-orbits.html

At first the remote sensing devices recorded photographic images on film (taken by cameras) or traces printed onto paper rolls (sonar devices), but because there images were fixed and could not be subject to further manipulation they are being replaced with modern systems where the sensors record their information in digital format, often as digital images. A digital image is made up of numbers, which represent image attributes such as brightness, color or radiance at different wavelengths, and position location for each point or picture element in the image. A raster image (digital image) is made up of pixels arranged in rows and columns. The smallest sized picture element on an image is called a pixel and the spatial resolution, which is one of the main characteristics of a raster image, corresponds to the size of each of the image's pixels. Remote sensors measure differences and variations of the electromagnetic radiation of resolutions (spatial, temporal, spectral, and radiometric) each of which characterize the accuracy and usefulness of remote sensors to habitat mapping.

The four main characteristics of a satellite sensor are the following;

The **<u>Spatial resolution</u>**, which can be defined as the smallest discernible detail in an image (Gonzalez, Woods). For digital images, this refers to the diameter of the ground resolution cell corresponding to a single pixel (fig. 14). It has to be mentioned that the number of the pixels does not matter in the spatial resolution. Satellite data on the basis of their spatial resolution are classified as:

- Very high spatial resolution (0.6-4m)
- High spatial resolution (4-30 m)
- Medium spatial resolution (50-250 m)
- Low spatial resolution (250 > 1000m).
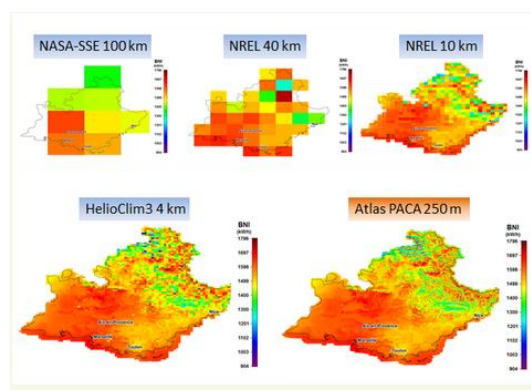
Fig. 14: Visualisation of the impact of the spatial resolution on maps of solar radiation

The **<u>Spectral Resolution</u>**, which describes the ability of a sensor to define fine wavelength intervals. The finer the spectral resolution, the narrower the wavelength ranges for a particular channel or band. Their purpose is to capture the differences in the reflection characteristics of different surfaces. Unlike the human eye which can only recognize the visible spectrum of light, a satellite sensor is able to measure radiation in many spectral different bands. The majority of passive Earth observation satellites have between three and eight bands of regions called multispectral. Hyper spectral sensors have more than 100 bands, several thousands of bands on typical of interferometry sensors (ultra-spectral).

The **<u>Temporal resolution</u>**, which is the time interval between two measurements performed on the same area by a satellite sensor. It is also called repetition rate and is determined by the altitude and orbit of the satellite as well as by its sensor characteristics (viewing angle).The temporal resolution is reduced by clouds which present selected visible or emitted infrared radiation, that does not penetrate through clouds, to reach the sensor. Areas of the Earth covered by clouds cannot be properly depicted when a satellite passes over them.

Satellite data on the basis of their temporal resolution are classified as:

- High temporal resolution: < 24 hours - 3 days
- Medium temporal resolution: 4 - 16 days
- Low temporal resolution: > 16 days

The last one is the **<u>Radiometric resolution,</u>** which refers to number of grayscale levels (binary bit-depth) at which data is recorded by a particular sensor. The binary bit-depth (fig. 15) is typically expressed in the following ranges of grayscale levels: 8-bit (0–255), 10-bit (0–1,023), 11-bit (0–2,047), 12-bit (0–4,095) and 16-bit (0–65,535). The finer or the higher the radiometric resolution is, the better small differences in reflected or emitted radiation can be measured, and the larger the volume of measured data will be.
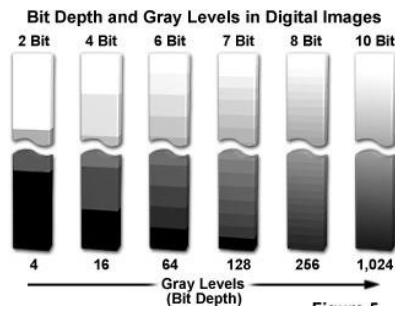
Fig. 15: The bit-depth and gray levels in digital images

Source: http://www.olympusmicro.com/primer/digitalimaging/digitalimagebasics.html

2.2 Using satellite images to investigate Geothermal Activity

Thanks to several satellite platforms orbiting around the Earth offering global coverage, continuity of observations and multispectral data generally at low costs, satellite remote sensing techniques represent an important tool for studying and monitoring several natural/environmental phenomena. In particular, the synoptic view offered by satellite systems (enabling the analysis of very large areas filling gap in the ground-based measurements) along with the high frequency of observations (up to 15 minutes for geostationary satellite platforms like MSG-SEVIRI) make them particularly suited for investigating among the others the geothermal fields. In more detail, satellite observations may be used to map surface mineral indicators of active hydrothermal systems, to investigate surface thermal anomalies related to geothermal emissions and to measure the heat fluxes associated to geothermal resources (Howari, 2015).

Sensors like TM (Thematic Mapper) onboard LANDSAT 4 e 5 satellites (16-day repeat cycle) offering a spatial resolution of 30 m in the visible (VIS) and near infrared (NIR) bands and of 120 m in the thermal infrared region (TIR) were widely used for identifying hydrothermal minerals (e.g. Taranik, 1988; Yang et al., 1999). They may be used as a proxy for mapping fault and fractures associated to geothermal systems (e.g. Huntington, 1996; Martian et al., 2004). These minerals show typical spectral absorption features in the visible and infrared region because of electronic and molecular vibrations (e.g. iron oxides, clays, sulfates and carbonates have important absorption bands in the range 0.4-2.5 μm; Clark, 1999) which may be exploited to map active and fossil geothermal systems (Howari, 2015). It means that both multispectral and hyperspectral sensors (providing data in hundreds of spectral

bands of narrow bandwidths) may be used for recognizing areas of hydrothermal alteration mineralogy (e.g. Martini et al., 2004), to map geothermal indicator minerals and to delineate targets of a future geothermal exploration (e.g. Littlefield and Calvin, 2014).

The potential of TIR observations (in the range 8–12 μm) for detecting surface temperature anomalies associated with geothermal fields was assessed in some literature works (e.g. Vaughan et al., 2005). ASTER (Advanced Spaceborne Thermal Emission and Reflection Radiometer) which is a high resolution imaging instrument flying on the Terra satellite providing data with a spatial resolution of 90 m in the TIR bands was used for studying geothermal hot springs in the United States including those of the Yellowstone National Park (e.g. Hellman and Ramsey 2004). This important geothermal area was investigated even by Fred et al., (2008) using the ETM+ (Enhanced Thematic Mapper plus) sensor aboard LANDSAT 7 satellite offering seven spectral channels such as TM but with an improved spatial resolution (from 15 to 90 m). In addition, ETM+ data were analyzed even to estimate the geothermal heat flux associated to active mud volcanoes in Southeastern Alaska (Patrick et al. 2004).

Among the studies performed exploiting TIR radiances some authors used the AVHRR sensor (Advanced Very High Resolution Radiometer) aboard NOAA (National Oceanic and Atmospheric Administration) satellites for the geothermal zoning of Russia (e.g. Gorny et al., 1997). In spite of the low spatial resolution similar to AVHRR (i.e. 1 km at the nadir view), MODIS TIR data were analyzed to record background thermal radiance variations from March 2000 through December 2010 in the Yellowstone's geothermal area (Vaughan et al., 2012).

Hence, a number of satellite sensors with different features in terms of spectral, spatial and temporal resolution may be used for studying geothermal activity with the choice of data depending on parameter of interest (Table 3). The mapping of minerals at hydrothermal systems requires for instance the use of satellite data at high spectral and spatial resolution. On the other hand, for monitoring geothermal emissions at large-scale satellite sensors offering a good compromise between spatial and temporal sampling are required. In this context, the analysis of long time series of TIR MODIS radiances could provide information suited to detect changes in thermal emissions at hydrothermal systems (Vaughan et al., 2012). Moreover, time series of land surface

temperature (LST) MODIS data could be investigated for isolating geothermal anomalies from the seasonal LST variability (e.g. Miliaresis et al., 2009), with such investigation revealing the presence of geothermal targets in the Aegean Sea (Zouzias et al., 2011). A decorrelation stretch method of monthly averaged LST MODIS night imagery was recently proposed (Miliaresis, 2012a) recognizing a geothermal activity in the Afar Triple Junction (Eastern Africa) (Miliaresis, 2012b). Hence, when proper satellite-based methods are used the geothermal activity may be better investigated from space although some issues still remain (e.g. solar radiation, changes of vegetation cover, topography and meteorological conditions affecting the identification of geothermal anomalies when LST MODIS data are used; Stroppiana et al., 2014; Howari, 2015).

Sensor	Platform/Satellite	Spatial Resolution	Global Coverage	Swath Width
MODIS	Terra, Aqua	1km	4 times/day	2,330km
ASTER	Terra	90m	4-16 days	60km
AVHHR-1	NOAA 6,8,10, TIROS – N	1.1km	Less than 1 day	2,600km
AVHHR-2	NOAA 9-14	1.1km	Less than 1 day	3,000km
AVHRR-3	NOAA 15-19, Metop A,B	1.1km	Less than 1 day	3000km
ETM+	Landsat 7	60m	16 days	185km
TM	Landsat 5	120m	16 days	185km
TIRS	Landsat 8	100m	16 days	185km
ATSR-2	ERS-2	1km	3 days	512km
AATSR	Enisat	1km	35 days	500km
MERSI	FY-3A, FY-3B	250m	1 day	2,800km
IRMSS	CBERS-1,2,2b	160m	26 days	120km
IRSCAM	CBERS-3, 4, 4b	80m	26 days	120km
NIRST	Aquarius	351m	Less than	182-

			1-2 days	1,060km
InfaredCam	HJ-1B	300m	31 days	720km
BIRD	BIRD	370m	10 days	190km
VIIRS	Suomi NPP	1.6km	Less than 1 day	3,000km
TET-1	TET-1	356m	10 days	180km
CERES	Suomi NPP	20km	Less than 1 day	3,000km
IIR	Calipso	1km	16 days	64km
Crls	Suom NPP	14km	Less than 1 day	2,200km

Table 3: Sensors that are used mostly for the LST measurements and application

In this study, we evaluate the potential of a largely accepted multi-temporal method of satellite data analysis to investigate the geothermal fields characterizing the high enthalpy regions of Aegean Arc. The here presented study aims at better assessing the contribution that satellite observations may provide for monitoring a geothermal region of great interest not only for scientists but also for politicians. In fact, geothermal fields represent an important energetic resource for Greece. It is important to stress that up to now geothermal resources have been poorly exploited in this country also because of opposition of the local population (e.g. Mendrinos et al., 2012). Thus, apart from some low enthalpy geothermal resources used for greenhouse heating and balneological purposes (e.g. Andritsos et al., 2010), no geothermal electricity is produced in Greece in spite of high-enthalpy geothermal fields in the islands of Milos and Nisyros whose potential for power generation exceed 250MWe (Andritsos et al., 2015; Lund and Boyd, 2016)

The identification of surface thermal anomalies from space is based on Planck law (see equation (1)) according to each body having temperature above absolute zero emits electromagnetic radiation as a function of its temperature:

$$B_\lambda(T) = \frac{2\pi h c^2}{\lambda^5 (e^{hc/\lambda kT} - 1)}$$
(1)

Where $B_\lambda(T)$ [W m^{-2} μm^{-1}] is the thermal radiation emitted by the blackbody (i.e. an ideal radiators absorbing and re-emitting the entire energy incident upon it) at specific wavelength λ [μm], h is the Planck constant h=6.68x10^-34 Ws^2, c is the velocity of light, k is the Boltzmann's constant and it is k=1.38x10^-2 Ws/K, T is the absolute temperature and λ is the emission wavelength.

Fig. 8 displays the Planck curves for black bodies at different temperatures. As can be seen from the figure, the Sun emits the maximum of thermal radiation in the visible band (VIS) at around 0.5 μm. Magmatic bodies having temperature around 1000 K
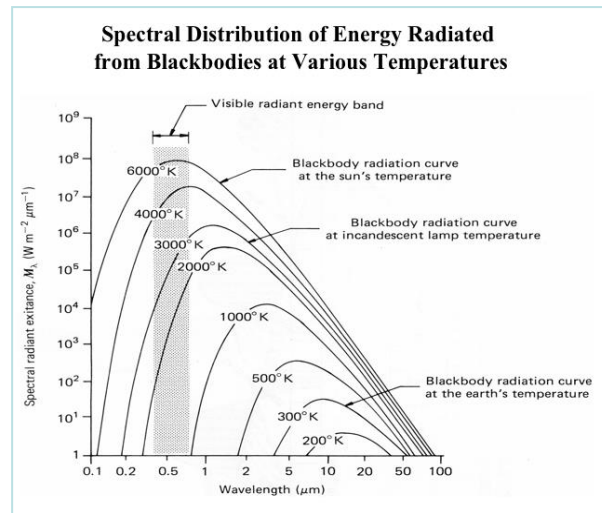
(e.g. lava flows) are more radiant in the Medium Infrared Region at around 3 μm wavelength (MIR). The Earth, having temperature around 300 K, reaches the peak of thermal emissions in the Thermal Infrared Region (TIR) around 10 μm wavelengths.

Fig 9: Planck curves for black bodies at different temperatures

The Wien Law describes the relation between body temperature (T) and wavelength (λ_{max}) at which the maximum spectral radiance is emitted.

$$\lambda_{max} = \frac{2898}{T} \tag{2}$$

Hence, as the temperature increase the maximum of thermal emission shifts to shorter wavelengths. Geothermal sources (having temperature ranges discussed in section 1.1) should be then potentially detectable by sensors having channels in the TIR band and more in particular in the spectral range 8-14 μm where an important atmospheric

window (i.e. a spectral region for which the atmosphere is relatively transparent) exists (fig. 16). In this spectral region (where aerosol absorption and scattering is generally negligible and ignored; Prata et al 1995), the water vapor is the main responsible for atmospheric effects. It varies on a short-time scale unlike other gases (e.g. O_3 and CO_2) that also influence the atmospheric transmission varying slowly (Dash et al., 2002).
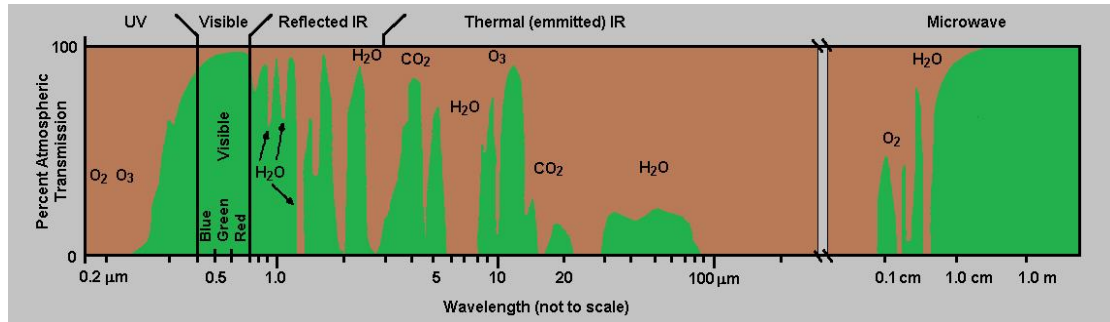
Fig. 16: Atmospheric windows with indication of absorbing molecules

Source: (http://www.oneonta.edu/faculty/baumanpr/geosat2/RS-Introduction/RS-Introduction.html)

As discussed in the previous section, a number of studies were performed to investigate geothermal fields in the TIR region using sensors like ETM+ and ASTER (e.g. Coolbaugh et al., 2007; Kienholz et al., 2009). Some of these studies quantified also the energy emitted by geothermal sources (e.g. Seielstad and Queen, 2009) based on Stefan-Boltzmann law:

$$Q = \sigma T^4 \tag{3}$$

Where Q is the radiant flux of the blackbody [W/m^2], T is the absolute kinetic temperature [K] and σ is the Stefan-Boltzmann constant [5.6697×10^{-8} W m^{-2} K^{-4}].

In spite of these studies, the investigation of geothermal fields from space is generally not a trivial task. In fact, the TIR radiance measured at the pixel level is generated by different sub-pixel surfaces (e.g. the geothermal source and the background at ambient temperature), with environmental factors like land cover, topography, albedo, and thermal inertia affecting the identification of subtle thermal anomalies related to sub-surface geothermal heating (Haselwimmer and Prakashm, 2013). Since these

factors influence the surface temperature changes (e.g. Taranik et al., 2009) proper corrections are required to mitigate their impact on identification of geothermal anomalies from space (i.e. reducing false positives associated to non-geothermal features) (e.g. Eneva et al., 2006; Coolbaugh et al., 2007).

As discussed in the previous section, several studies on geothermal fields were performed investigating changes in the land surface temperature. A detailed description of LST retrieval from space is reported in the next section.

2.3.: Land Surface Temperature (LST) measurements from satellite

The LST (i.e. the kinetic temperature of the earth's surface skin; Norman and Becker, 1995) is a key parameter in the physics of land surface processes from local through global scale (Andersonet al., 2008; Brunsell & Gillies, 2003; Karnieli et al., 2010, Kustes & Anderson, 2009, Zhang t al., 2008).
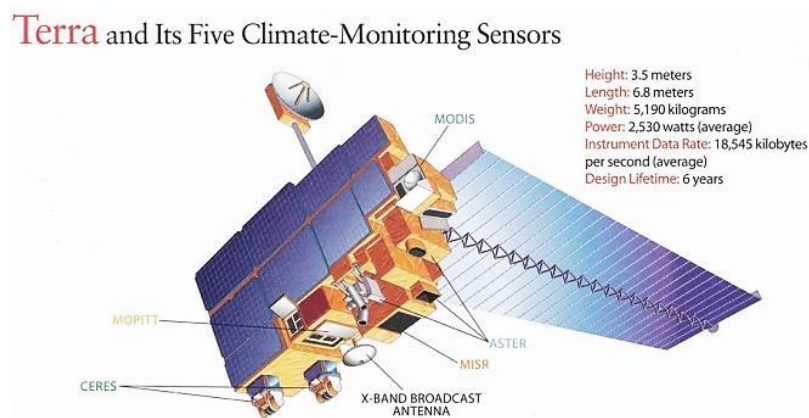
Fig. 17: The TERRA satellite and its five climate-monitoring sensors
Source: http://www.magnolia.com.ru/satellites/modis/

In fact, the LST is an important indicator of surface-atmosphere interactions as well as of the energy balance at the earth's surface (e.g. Sellers et al., 1988; Wang, 2009; Pinker et al., 2009). Since it provides information about different features as soil moisture, vegetation water stress and land surface disturbance accurate estimates of this parameter are crucial for applications in hydrology, meteorology and climatology (e.g. Sun, 2008; Gao et al., 2013; NOAA, 2016).

Satellite remote sensing enables estimations of the LST over wide areas (where there is a strong spatial heterogeneity in land surface characteristics, such as vegetation, topography and soil physical properties; Li et al., 2013), with a different temporal coverage. In particular, the LST may be retrieved analyzing both infrared and microwave satellite observations (Sun et al., 2006). The TIR-based LST retrievals are more accurate than microwaves ones because of smaller range of variation of land surface emissivity (LSE) in the TIR and due to the stronger dependence of the radiance on temperature (Sun, 2008).

Several methods have been up to now developed for estimating the LST using sensors like AVHRR and MODIS, with the aim of reaching an accuracy better than 1 K (Gao et al., 2013). These algorithms are generally classified as:

- Single-channel techniques
- Multi-angle methods
- Split-window (SW) algorithms
- Stepwise retrieval method

The single channel methods (e.g. Price 1983; Qin et al. 2001) were developed to retrieve LST from radiances measured in a single atmospheric window channel. This method required the knowledge of land surface emissivity as well as accurate atmospheric profiles to be applied (Gao et al., 2013). Multi-angle algorithms exploit the different signal absorption resulting from different atmospheric path-lengths associated to the observation of the same object under different viewing angles (e.g. Sobrino et al. 1996). These methods require a significantly longer atmospheric path for one of measurements along with the knowledge of the angular variation of the surface emissivity (e.g. Prata, 1993).

Split-window techniques analyze the different absorptions of the signal in the two adjacent spectral channels of sensors like AVHRR providing estimates of LST without requiring detailed atmospheric profiles. The basic split-window equation is:

$$T_s = T_{11} + a(T_{11} - T_{12}) + b \tag{4}$$

In this equation, T_s is the retrieved surface temperature, T_{11} and T_{12} are the brightness temperatures measured at 11 μm and 12 μm wavelengths (e.g. AVHRR channels 4

and 5), while the coefficient a and b taking into account the atmospheric conditions and the surface emissivity respectively. The spectral emissivity is defined as:

$$\varepsilon_\lambda = \frac{I_\lambda(T)}{B_\lambda(T)} \tag{5}$$

Where, $I_\lambda(T)$ is the spectral radiance emitted by an object at temperature T and wavelength λ, and $B_\lambda(T)$ is that emitted by a black body at the same wavelength and temperature.

Since equation (5) is ineffective at a global scale due to parameters that are valid only for the datasets used to derive them, several split window algorithms have been up to now developed to improve the retrieval of LST from space (Dash et al., 2002).

Among those methods, Wan and Dozier (1996) optimized the split window algorithm proposed by Becker and Li (1990) introducing some coefficients varying with satellite zenith angle (SZA), water vapor, and lower boundary air temperature.

$$T_S = C + \left(A_1 + A_2 \frac{1 - \varepsilon}{\varepsilon} + A_3 \frac{\Delta\varepsilon}{\varepsilon^2} \right) \frac{T_{11} + T_{12}}{2} +$$
$$\left(B_1 + B_2 \frac{1 - \varepsilon}{\varepsilon} + B_3 \frac{\Delta\varepsilon}{\varepsilon^2} \right) \frac{T_{11} - T_{12}}{2} \tag{6}$$

Where, $\varepsilon = (\varepsilon_{11} + \varepsilon_{12})/2$ and $\Delta\varepsilon = \varepsilon_{11} - \varepsilon_{12}$. In equation (6), the coefficients A_i, B_i, and C depend on viewing zenith angle as well as on ranges of the air surface temperature and column water vapor. The generalized split-window algorithm described by equation (6) K is used to retrieve the level-2 MODIS LST products (i.e. MOD11_L2) (National Aeronautics and Space Administration, 2016a) which are described in the next section.

Other authors introduced nonlinear split window methods to improve the accuracy of LST retrievals incorporating the LSEs into the used coefficients (e.g. Sobrino et al., 1994), integrating both the LSE and the water vapor corrections (e.g. Sobrino and Raissouni 2000), or take into account even the viewing zenith angle (e.g. Sobrino and Romaguera, 2004; Atitar and Sobrino; 2009).

The stepwise retrieval methods are based on two consecutive steps. The first one foresees the retrieval of LSE from visible/near-infrared (VNIR) measurements or from atmospherically corrected MIR and TIR radiances estimated at ground level. In the second step, the LST is estimated using single channel, multi-angle or split

window methods. It should be noted that that together with methods described above, the LST retrieval may be performed using other satellite-based algorithms with different advantages and limitations (e.g. see Li et al., 2013). Main issues affecting the estimates of LST from space are discussed in the next paragraph.

2.3.1 Difficulties in estimates the LST by satellite and solutions

The satellite-based estimates of LST require the radiometric calibration, the use of a cloud-screening procedure and the application of atmospheric, emissivity and topography corrections to be performed (Price, 1984; Wan and Li 1997; Liang 2001, 2004). Cloud screening procedures may strongly influence the LST retrievals such as the accuracy of radiometric calibration. In particular, cirrus clouds may significantly affect the estimates of LST when they are performed using TIR data (Fan et al., 2015a). Most algorithms do not retrieve the LST in the presence of cloudy pixels. However, when cloudy-sky is misinterpreted as a clear-sky large errors affect the LST estimations from space (Xu et al., 1991). A three-channel LST retrieval algorithm analyzing the MIR radiance was developed for correcting the LST errors related to clouds, taking into account the variations in the cirrus optical depth, effective radius and top height. Nevertheless, this method was applicable only in nighttime conditions (Fan et al., 2015b). Afterwards, a daytime LST retrieval algorithm under cirrus cloudy conditions was proposed and tested, showing that improvements in the estimates of LST are possible also in daylight conditions (Fan et al., 2015a).

Atmosphere corrections generally represent the first correction step implemented within the LST retrieval algorithms (e.g. Tang and Li, 2013). In fact, since the atmosphere affects the radiance measured by satellite, the atmospheric corrections are strongly required to increase accuracy of LST estimations. These procedures require accurate vertical profiles of atmospheric water vapor and temperature to be performed (Perry and Moran, 1994). Moreover, the effect of aerosol on LST retrieval if relatively small if compared to water vapor (the transmittance of aerosol in the MODIS TIR bands is generally in the range of 0.95-0.98; Wan, 1999). Hence, the LST retrieval algorithms generally consider an average aerosol distribution and a constant aerosol loading. However, for better estimating the LST in the presence of high aerosol loading these methods need to be improved correcting for the aerosol effect (e.g. Tang and Li, 2013; Gao et al., 2015).

Another important issue affecting satellite-based algorithms developed for retrieving the LST is the emissivity of land surfaces (Wan, 1999). In general, the efficiency of single channel methods as well as of split-window methods depends on the accuracy of surface emissivity (e.g. they do not perform well in semi-arid and arid regions because of significant variations of this parameter in both space and time; Wan et al., 2002). Hence, inaccuracies in the emissivity values may introduce large errors in the estimates of LST. Becker (1987) showed for instance that the effect of land surface emissivity on estimates of LST performed using split window methods is particularly significant. Several techniques have been developed to retrieve the emissivity from satellite records (e.g. see Dash et al., 2002; and reference herein), with studies performed to assess their efficiency revealing different estimation errors (e.g. because of instrumental noise and calibration error, uncertainties in the estimation of downwelling irradiance and atmospheric correction errors; e.g. Li et al. 1999). It is worth mentioning that a few methods do not require a priori knowledge of emissivity, performing simultaneous retrievals of LST and LSE.
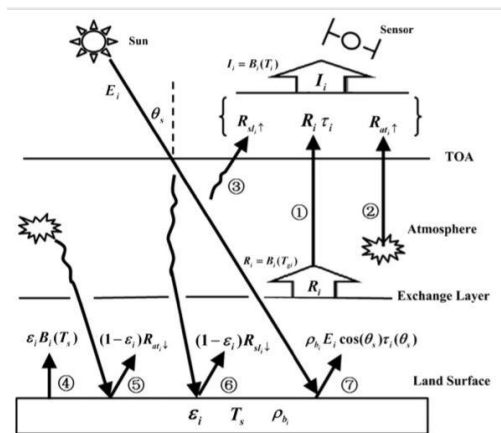
Fig.18:   The Land Surface Temperature (LST) working system
Source: D. Zougias, George Ch. Miliaresis, K. St. Seymour, (2010),
Probable Regional geothermal field reconnaissance in the Aegean
region from modern multi-temporal night LST imagery

Among them, the algorithm proposed by Wan and Li (1997) analyzing pairs of day/night observations in seven MODIS channels and assuming that the LSE is temporally invariant is used to for simultaneously retrieving surface temperatures and band-averaged emissivity. This method (which is used to generate one of MODIS

products described in the next paragraph) increases performance of a previous algorithm (Li and Becker, 1993) estimating both LSE and LST using pairs of day/night co-registered AVHRR images.

Along with issues discussed above, the validation of LST estimations from space (the temperature-based method and the radiance-based method are commonly used to validate the satellite-based LST products; Li et al., 2014) is another important factor that needs to be taken into account. Validation is challenging because of difficulty of performing in situ LST measurements as well of obtaining LST data at the scale of single image pixel. Moreover, the land surface temperature vary significantly in both space and time (e.g. Prata et al., 1995) generally limiting the ground-based validation analyses to relatively homogeneous land surfaces (Li et al., 2013).

2.4.: Choosing the MODIS-LST product
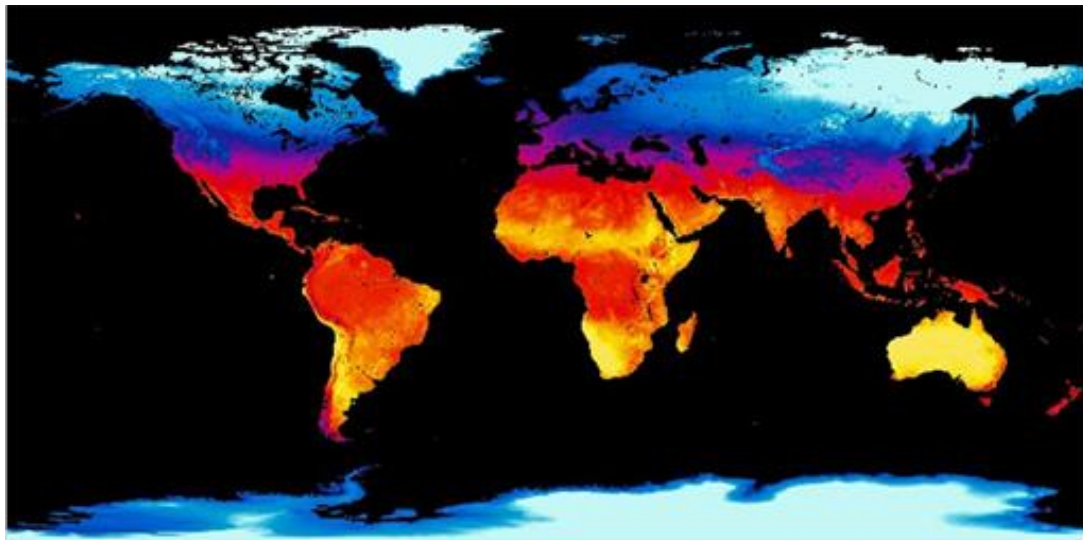
Fig. 19: MODIS LST global image from NASA
Source: http://neo.sci.gfsc.nasa.gov/blog/category/new-datasets/

MODIS aboard Terra (originally known as EOS AM-1) and Aqua (originally known as EOS PM-1) satellites represents an important instrument for global studies of atmosphere, land, and ocean processes (Salomonson et al., 1989). This sensor (whose viewing swath is 2330 km wide and the revisit cycle is about one to two days) offers 36 spectral channels (see table X) with a different spatial resolution, respectively of 250 m (bands 1-2), 500 m (bands 3-7), and 1 km (bands 8-36). Channels 1-19 and channel 26 are located in the VIS and NIR (Near Infrared Region), while the other

spectral channels are located in the MIR and TIR bands. In more detail, channels 20, 22, 23, 29, 31-33 are used for correcting atmospheric effects and for retrieving surface emissivity and temperature (Wan et al. 1999).

The MODIS land surface temperature and emissivity (LST and LSE) standard products (i.e. MOD11 from Terra and MYD11 from Aqua) are generated on a global scale using three different algorithms. Specifically, the generalized split window algorithm is used to generate the LST data at 1 km resolution (MOD11_L2). The day/night algorithm produces the LST and LSE data at ~5 km (C4) and ~6 km (C5) resolution (MOD11_B1), while a product based on the ASTER Temperature Emissivity Separation (TES) algorithm (MOD21_L2) is used for LST and emissivity estimations in three TIR channels at 1 km spatial resolution (National Aeronautics and Space Administration, 2016b). The generalized split window algorithm (see equation (6)) has been validated by MAS (MODIS Airborne Simulator) data and field measurements since 1995 (Wan and Dozier, 1996) for correcting atmospheric and emissivity effects. In most cases, its accuracy is better than 1 K (Wan et al., 1999). The day/night LST algorithm was validated by MAS data and field measurement campaigns conducted in 1996-1998.
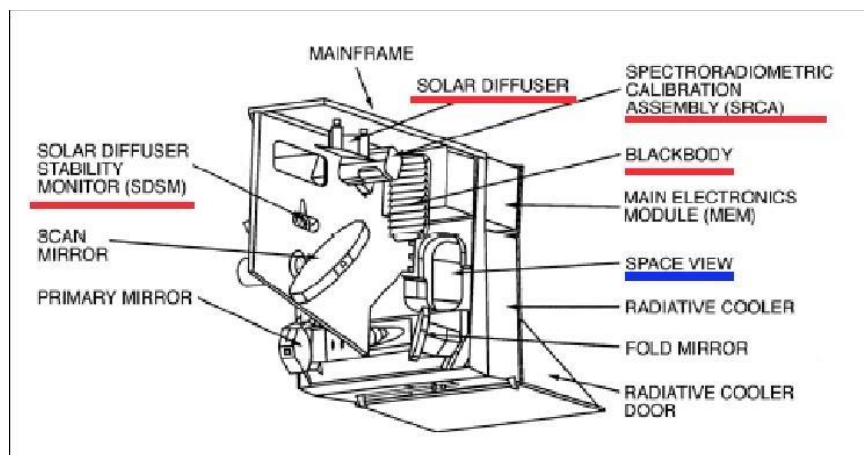
Fig.20: Major elements of the MODIS Instrument (credits NASA)

Source: https://directory.eoportal.org/web/eoportal/satellite-missions/content/-/article/terra-mission

The MODIS LST products are archived in Hierarchical Data Format - Earth Observing System (HDF-EOS) format files. HDF, developed by the NSCA, is the standard archive format for EOS Data Information System (EOSDIS) products.

In this thesis, we have analyzed the MODIS Land Surface Temperature and Emissivity Daily L3 Global 1 km (MOD11_A1) products (i.e. the version 005 (V5) available from March 5, 2000 for investigating possible geothermal anomalies at AVA. The MOD11_A1 represents a gridded version of MOD11_L2 with pixels that are projected to Earth locations on a sinusoidal mapping grid (Wang et al., 2008). This product has a spatial resolution of 1 km and guarantees an accuracy of 1 K under clear-sky conditions (e.g. Wan and Dozier, 1996; Wan 2006) . In fact, the retrieved LST is not mixed with cloud-top temperature and cloudy pixels are skipped in the LST processing using the MODIS cloud mask product (MOD35_L2 from Terra MODIS or MYD35_L2 from Aqua MODIS) (Wan, 2008). The accuracy of both MOD11_L2 and MOD11B1 LST products was assessed only for surfaces having a known emissivity. Indeed, the land surface emissivity is usually unknown and its retrieval on a global scale is difficult Wang et al., 2008).

It is important to stress that the MOD11_A1 product described above has been processed here for the first time in multi-temporal sequence according to the well-established RST (Robust Satellite Techniques; Tramutoli 1998; 2007) scheme. This multi-temporal method of satellite data analysis whose successful applications for detecting thermal anomalies related to volcanic eruptions (e.g. Pergola et al., 2004; 2008; 2015; Lacava et al., 2014; Marchese et al., 2011; 2012; 2014) and seismic activity (e.g. Tramutoli et al., 2005; Aliano et al., 2008; Genzano et al., 2015; Lisi et al., 2015), are shown in several literature studies, is discussed in detail in the next section.

Primary use	Band	Bandwith	Spectral Radiance	Required SNR
Land/Cloud/Aerosols Boundaries	1	620 - 670	21.8	128
	2	842 – 876	24.7	201
Land/Cloud/Aerosols Properties	3	459 – 479	35.3	243
	4	545 – 565	29.0	238
	5	1230 – 1250	5.4	74
	6	1628 – 1652	7.3	275
	7	2105 – 2155	1.0	110
Ocean Color	8	405 – 420	44.9	880

Phytoplankton Biogeochemistry	9	438 – 448	41.9	838
	10	483 – 493	32.1	802
	11	526 – 536	27.9	754
	12	546 – 556	21.0	750
	13	662 – 672	9.5	910
	14	673-683	8.7	1087
	15	743-753	10.2	586
	16	863-877	6.2	516
Atmospheric Water Vapor	17	890-920	10.0	167
	18	931-941	3.6	57
	19	915-965	15.0	250
Surface/Cloud Temperature	20	3.660 – 3.840	0.45(300K)	0.05
	21	3.929 – 3.989	2.38(335K)	2.00
	22	3.929 – 3.989	0.67(300K)	0.07
	23	4.020 – 4.080	0.79(300K)	0.07
Atmospheric Temperature	24	4.433 – 4.988	0.17(250K)	0.25
	25	4.482 – 4.549	0.59(275K)	0.25
Cirrus Clouds Water Vapor	26	1.360 – 1.390	6.00	150(SNR)
	27	6.535 – 6.895	1.16(240K)	0.25
Cloud Properties	28	7.175 – 7.475	2.18(250K)	0.25
	29	8.400 – 8.700	9.58(300K)	0.05
Ozone	30	9.580 – 9.880	3.69(250K)	0.25
	31	10.780–11.280	9.55(300K)	0.05
Surface/Cloud Temperature	32	11.770–12.270	8.94(300K)	0.05
	33	13.185-13.485	4.52(260K)	0.25
Cloud Top Altitude	34	13.485-13.785	3.76(250K)	0.25
	35	13.785-14.085	3.11(240K)	0.25
	36	14.085-14.385	2.08(220K)	0.35

Table 4: The 36 bands of MODIS

Source: http://modis.gsfc.nasa.gov/about/specifications.php

SDS	Units	Data Type	Fill Value	Valid Range	Scale Factor	Additional Offset
Daytime Land Surface Temperature	Kelvin	16-bit unsigned integer	0	7500-65535	0.02	NA
Daytime LSTE quality control	Bit-Field	8-bit unsidned integer	' '	0-255	NA	NA
Daytime LST observation time	Hours	8-bit unsidned integer	0	0-240	0.1	NA
Daytime LST view zenith angle	Degrees	8-bit unsidned integer	255	0-130	1.0	-65.0
Nighttime Land Surface Temperature	Kelvin	16-bit unsidned integer	0	7500-65535	0.02	NA
Nighttime LSTE quality control	Bit-Field	8-bit unsidned integer	' '	0-255	NA	NA
Nighttime LST observation time	Hours	8-bit unsidned integer	0	1-240	0.1	NA
Nighttime LST view zenith angle	Degrees	8-bit unsidned integer	255	0-130	1.0	-65.0

Band 31 emissivity	None	8-bit unsidned integer	0	1-255	0.002	0.49
Band 32 emissivity	None	8-bit unsidned integer	0	1-255	0.002	0.49
Daytime clear-sky coverage	None	16-bit unsidned integer	0	1-65535	0.0005	NA
Nighttime clear-sky coverage	None	16-bit unsidned integer	0	1-65535	0.0005	NA

Table 5: Terra/MODIS V005 MOD11A1 LST/E (1 Km) Science Data Set Layers

Source: https://lpdaac.usgs.gov/dataset_discovery/modis/modis_products_table/mod11a1

band	bandwidth (nm)	IFOV	primary use	band	bandwidth (µm)	IFOV	NEΔT (°K)	primary use
1	620- 670	250m	L	20	3.660-3.840	1km	0.05	O, L
2	841- 876	250m	A, L	21	3.929-3.989	1km		fire, volcano
3	459- 479	500m	L	22	3.929-3.989	1km	0.07	A, L
4	545- 565	500m	L	23	4.020-4.080	1km	0.07	A, L
5	1230-1250	500m	L	24	4.433-4.498	1km	0.25	A
6	1628-1652	500m	A, L	25	4.482-4.549	1km	0.25	A
7	2105-2155	500m	A, L	27	6.535-6.895	1km	0.25	A
8	405- 420	1km	O	28	7.175-7.475	1km	0.25	A
9	438- 448	1km	O	29	8.400-8.700	1km	0.05	L
10	483- 493	1km	O	30	9.580-9.880	1km	0.25	ozone
11	526- 536	1km	O	31	10.780-11.280	1km	0.05	A, L
12	546- 556	1km	O	32	11.770-12.270	1km	0.05	A, L
13	662- 672	1km	O	33	13.185-13.485	1km	0.25	A, L
14	673- 683	1km	O	34	13.485-13.785	1km	0.25	A
15	743- 753	1km	O	35	13.785-14.085	1km	0.25	A
16	862- 877	1km	O	36	14.085-14.385	1km	0.35	A
17	890- 920	1km	A					
18	931- 941	1km	A					
19	915- 965	1km	A					
26	1360-1390	1km	cirrus					

Note: A - atmospheric studies; L - land studies; O - ocean studies.

Table 6: Specifications of the EOS MODIS bands
Source: MODIS Level 1B Algorithm Theoretical Basis Document, 1995,
NASA/GSFC, Greenbelt, MD

CHAPTER 3

The Robust Satellite Technique (RST)

FOR VOLCANIC/GEOTHERMAL

FIELDS ANOMALIES DETECTION

In this chapter I will refer to the RST analysis and I will briefly describe the procession that was followed step-by-step until the final results for the 12 years of data, commenting each time the results and the thoughts for moving from one step to the other. Along with that there will be mentioned the toolboxes that were created on ArcMap 10.1 specifically for the imaging procession and the RST analysis.

3.1.: The Robust Satellite Technique (RST) general approach

The methodologies that were used in order to detect the thermal anomalies was at first the ALICE index and then the Robust satellite Techniques (RST) (Tramutoli et al., 2005; 2007), which is a multi-temporal scheme of satellite data analysis that it seems to be suitable for recognizing space-time anomalies in the satellite observational-field (Lisi et al., 2010). The Robust AVHRR Techniques (RAT) (Tramutoli et al., 1998) is actually the first name and the first version of the RST techniques, but since the approach could be implied for a numerous of sensors the name changed to RST. In fact RST is a change detection algorithm (Tournaviti et al., 2013) that is based on the logic that the space-time transient anomalies must be detect due to respect to the normal behavior (in unperturbed condition, i.e. in the absence of the considered phenomenon) of the measured signal (Lisi et al., 2010). For this reason an analysis at pixel level of historical data (multi-year imagery) has to be applied with specific homogeneous criteria, such are the same sensor, the same spectral bands & channels, the same geographical area and the same recording period (same day and same month for each year).

Two of the main positive factors that the RST methodology has are: (i) the reduce of the "natural noise" (Lisi et al., 2010) (atmosphere, different ground cover lands - that changes both in the time and space - topography and climate conditions) and (ii) that there is no need of ground-based measurements, which in many cases, such in ours with the geothermal activity, is almost impossible to be applied.

At first, an index named ALICE (Absolutely Local Index of Change of the Environment) is computed by RAT to this aim, and defined in its general mathematical formulation as (Eleftheriou et al., 2014):

$$\otimes_V(x,y,t) = \frac{[V(x,y,t) - V_{REF}(x,y)]}{\sigma_V(x,y)} \qquad (6)$$

Where, <u>V(x,y,t):</u> is the signal measured at time t for each pixel (x, y) of the satellite image to process, <u>V_{REF}(x,y):</u> is the expected value, which is generally expressed as the temporal mean & <u>σ(x, y):</u> is the natural variability of the signal (i.e. the temporal standard deviation). In this way, the ALICE index provides at a pixel-level an estimate of the difference between the signal V(x,y,t) observed at time t and its expected median value μV(x,y), weighted by the historically observed signal variability σV(x,y) which includes all the possible noise sources which are not related to the event to be monitored (Lisi et al., 2010) and thus, we can understand that as higher are the ALICE index values, the stronger will be the anomaly intensities (Eleftheriou et al., 2014). By using this index we can succeed the reducing of the "noise" in our TIR measurements that have been collected by the satellite. The robustness of such an approach is intrinsic, because in order to identify a signal as "anomalous" the value must be higher than the expected for a specific condition of observation, and only if this deviation is significantly higher than the natural signal variability. Up to now, the technique has been applied with success to major natural and environmental hazards (Lisi et al., 2010). Two of them are; the volcanic risk (Pergola et al., 2001; Tramutoli et al., 2001b; Di Bello et al., 2004; Pergola et al., 2004a, b; Bonfiglio et al., 2005; Filizzola et al., 2007; Marchese et al., 2006;) to the hydrological risk (Tramutoli et al., 2001c; Lacava et al., 2005; Lacava et al 2006; to the fire risk in Cuomo et al., 2001).

In many cases in the measurements of TIR anomalies the unexpected climatological changes was still affecting the results, even after the computation of the ALICE index. For this reason some scientists were using the equation (7) of the so-called of RETIRA index (Robust Estimator of TIR Anomalies):

$$\otimes_{\Delta T}(r,t') = \frac{\Delta T(r,t\prime) - \mu_{\Delta T}(r)}{\sigma_{\Delta T}(r)} \qquad (7)$$

Where:

(i)   r=(x,y) represents the coordinates of each pixel on the satellite image and *t'* is the time of acquisition of the satellite image at hand, with *t'*∈ τ, where τ

defines the homogenous domain of satellite imagery collected in the same time (hour) of the day and the same period (month) of the year.

(ii) $\Delta T(r,t') = T(r,t')-T(t')$ is the difference between the current TIR signal value $T(x,y,t)$ measured at location r, and its spatial average $T(t)$, computed in place on the image at hand considering only cloud-free pixels, all belonging to the same, land or sea -according to where the r is located over the area-, class in the investigated area.

(iii) $\mu_{\Delta T}(r)$ refers to time average and $\sigma_{\Delta T}(r)$ to standard deviation of $\Delta T(r,t')$ at location r, computed on cloud-free records from satellite belonging to selected homogenous datasets ($t' \in \tau$).

In this way, the ALICE – RETIRA ($\otimes$ (r, t')) index gives us the signal (S) that has to be investigated for its possible relation with geothermal activity, by comparing the llocal (spatial-temporal) excess of the current ΔT (r, t') signal with its historical mean value and weighted by its historical variability $\sigma V(x,y)$ at the considered location. The considered location includes all the possible noise sources which are not related to the event to be monitored. The choice of differential variable $\Delta T(r,t)$, instead of $T(r,t)$, is expected to reduce possible contributions (e.g. occasional warming) due to day-to-day and/or year-to-year climatological changes and/or season time-drifts (Lisi e al., 2010). In this way someone is able to reduce the problem of noise within the TIR measurements acquired by satellite. Both $\mu\Delta T(r)$ and $\sigma\Delta T(r)$ are computed for each location r, processing several years of historical satellite records acquired in similar observational conditions. (Eleftheriou et al., 2014). The signal (S) is always evaluated by comparison with the corresponding natural/observational noise (N), represented by standard deviation, $\sigma\Delta T(r)$. In this way, the intensity of anomalous TIR transients can be evaluated in terms of S/N ratio by the $\otimes$(r, t') index. Tramutoli et al., (2001) reported that, the use of RETIRA index should highlight the presence of thermal anomalies effectively independent from the known sources of natural/observational noise, also in very low intensity.

3.2.: MODIS data pre-processing

After the decision of the application, the testing area, the time period, the specific instrument/satellite and product we had to download our data (4353 TIR images) from NASA's REVERB website and do the pre-processing in order to prepare the images for the RST analysis. The total number of the images can be seen in the table 7.

The historical data-set for the calculation of the ALICE – LST and RETIRA – RST should be at least five years. We have chosen 12 years of homogenous satellite data (same year, same month, same platform/product etc.). All of the images are taken at night in order to reduce the weather influences and more specifically at the same time of night.

For the pre-processing of the images, at first, we isolated the "Nighttime and Surface Temperature" layer dataset and at the same time we cropped the images in order to isolate the land of Turkey. A new toolbox with the name "BAND4_oκ2.tbx" (fig. 21) has been created to fulfil this two actions.
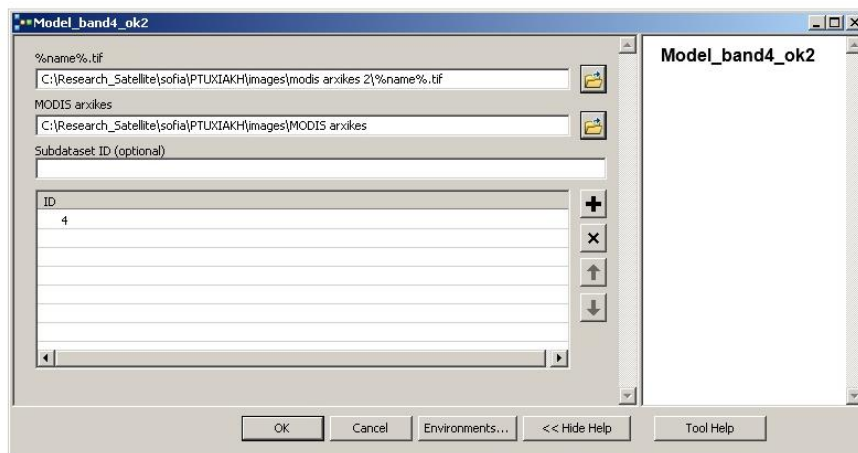
Fig. 21: Toolbox "BAND4_ok2"

It should be noticed that for the correct computing of the indexes no cloudy pixels should be involved. In our application with the MOD11A1 product the cloudy pixels are already filtered by NASA appears as "NO DATA". While working on ArcMap we just had to choose the selection of "ignore NO DATA" in all of our computations.

	'03	'04	'05	'06	'07	'08	'09	'10	'11	'12	'13	14	
Jan.	31	31	31	31	31	31	31	31	31	31	31	31	**372**

Feb.	27	28	28	28	28	29	28	28	28	29	28	28	**337**
Mar.	31	30	31	31	31	30	31	31	31	30	31	31	**369**
Apr.	30	30	30	30	30	30	30	30	30	30	30	30	**360**
May	31	31	31	31	31	31	31	31	31	31	31	31	**372**
June	30	30	30	30	30	30	30	30	30	30	30	30	**360**
July	31	31	31	31	31	31	31	30	31	31	31	31	**371**
Aug.	31	31	31	31	31	31	31	31	31	31	31	31	**372**
Sept.	30	30	30	30	30	30	30	30	30	30	30	30	**360**
Oct.	31	31	31	31	31	31	31	28	31	30	31	31	**368**
Nov.	30	30	30	30	29	30	30	29	30	30	30	26	**354**
Dec.	23	30	31	31	31	27	31	31	31	30	31	31	**358**
Total	**356**	**363**	**365**	**365**	**364**	**361**	**365**	**361**	**365**	**363**	**365**	**360**	<u>**4353**</u>

Table 7: Total amount of data

3.3: RST-ALICE analysis

After the creation of the historical data-sets that we described in the previews paragraph, a calculation and detection of the thermal anomalous pixels in our satellite images should be done. The primal step is the creation of the reference fields of each cloud-free pixel of homogenous data (same hour, same day and same month) for all the time-period (x12 months) in order to create 12 maps for each calendar month of the year with the "normality" (mean) of each pixel and 12 maps of the standard deviation.

The "cell statistics" toolbox (fig. 22) was used for the calculation of the "mean" and the "standard deviation" values. By clicking the 'Ignore NoData in calculations" we succeed to have only cloud-free pixels in our calculations.
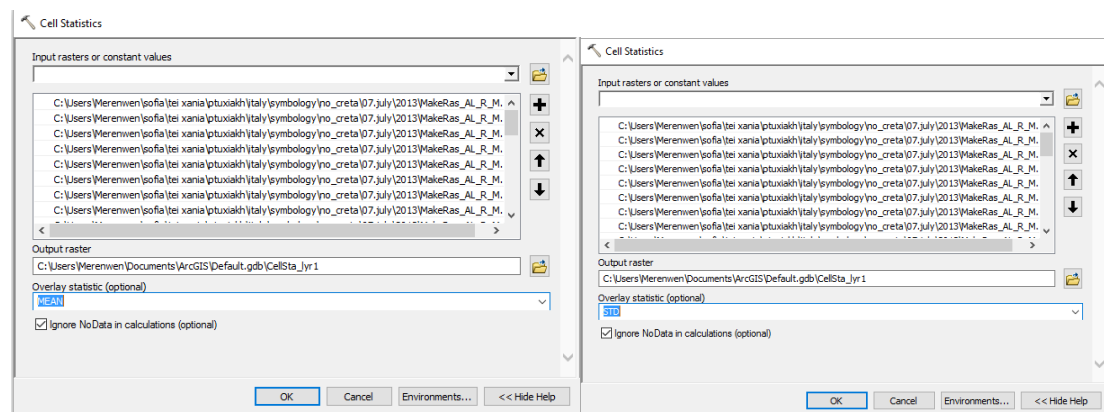
Fig. 22: The "Cell Statistics" toolbox for the calculation of the mean (left image) and the calculation of the standard deviation (right image)

The first application happened with the ALICE index (equation 6). For the calculation of the index an identification of the temporal mean maps should carried out, along with the general mean and standard deviation maps that were created before.

A monthly and daily approach was carried out and it is briefly described in the following two paragraphs.

3.3.1: Monthly Analysis

Zouzias et al., (2010) successfully identified geothermal fields in the Aegean region by using MODIS-LST monthly imagery. In our attempt to recognize the anomalies that occur on the already known geothermal/volcanic fields and in order to reduce the weather and seismic effects, we also made a monthly investigation but by using a different approach with the calculation of the ALICE index (equation 8).

$$\otimes_V(x,y,t) = \frac{[V_{mean}(x,y,t) - V_{REF}(x,y)]}{\sigma_V(x,y)} \qquad (8)$$

Where, "$V_{mean}(x,y,t)$" is the temporal mean of each month of each year.

Once more the "cell statistics" toolbox was used for the creation of the temporal mean maps (12x12 maps). The ALICE index determined with the "raster calculator" toolbox (fig. 23) and indicative the years 2006 and 2013 are shown in the fig.24 and fig. 25.
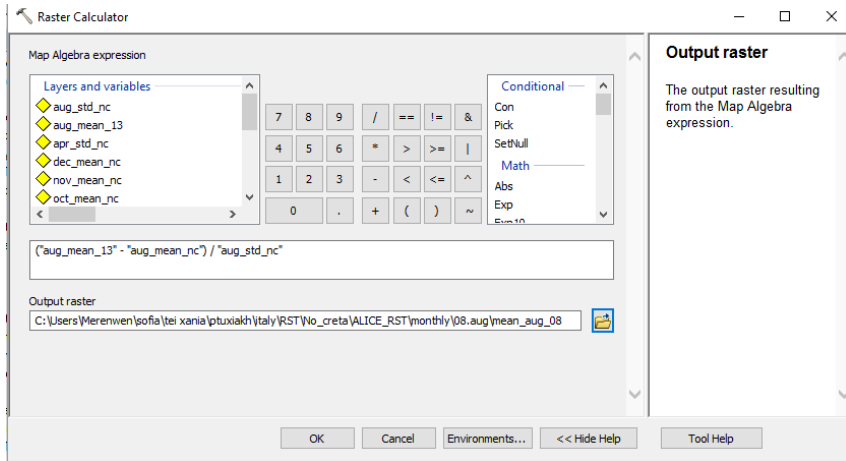
Fig. 23: The "Raster Calculator" toolbox for the determination of ALICE index
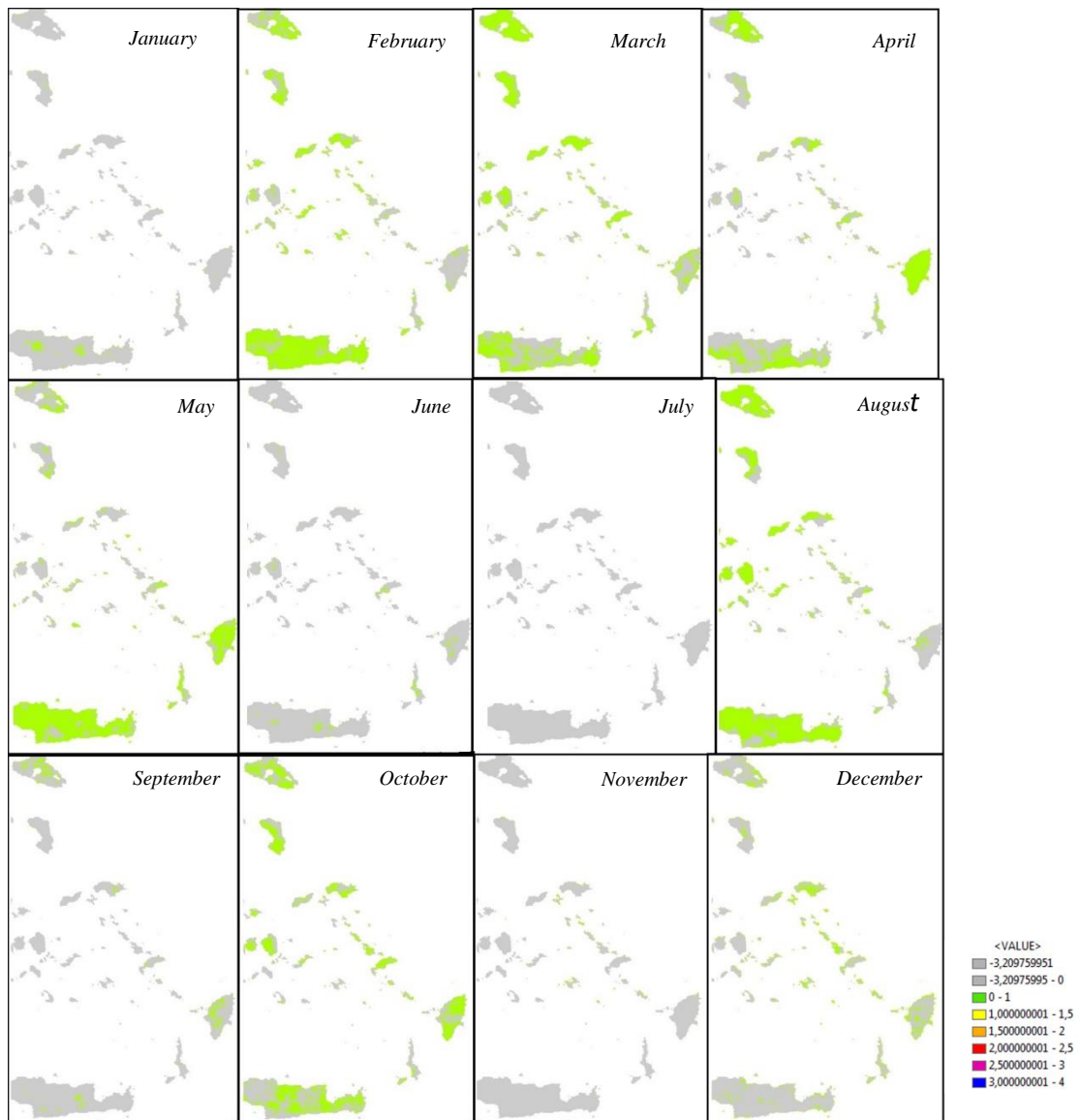
Fig. 24: Monthly ALICE maps for 2006
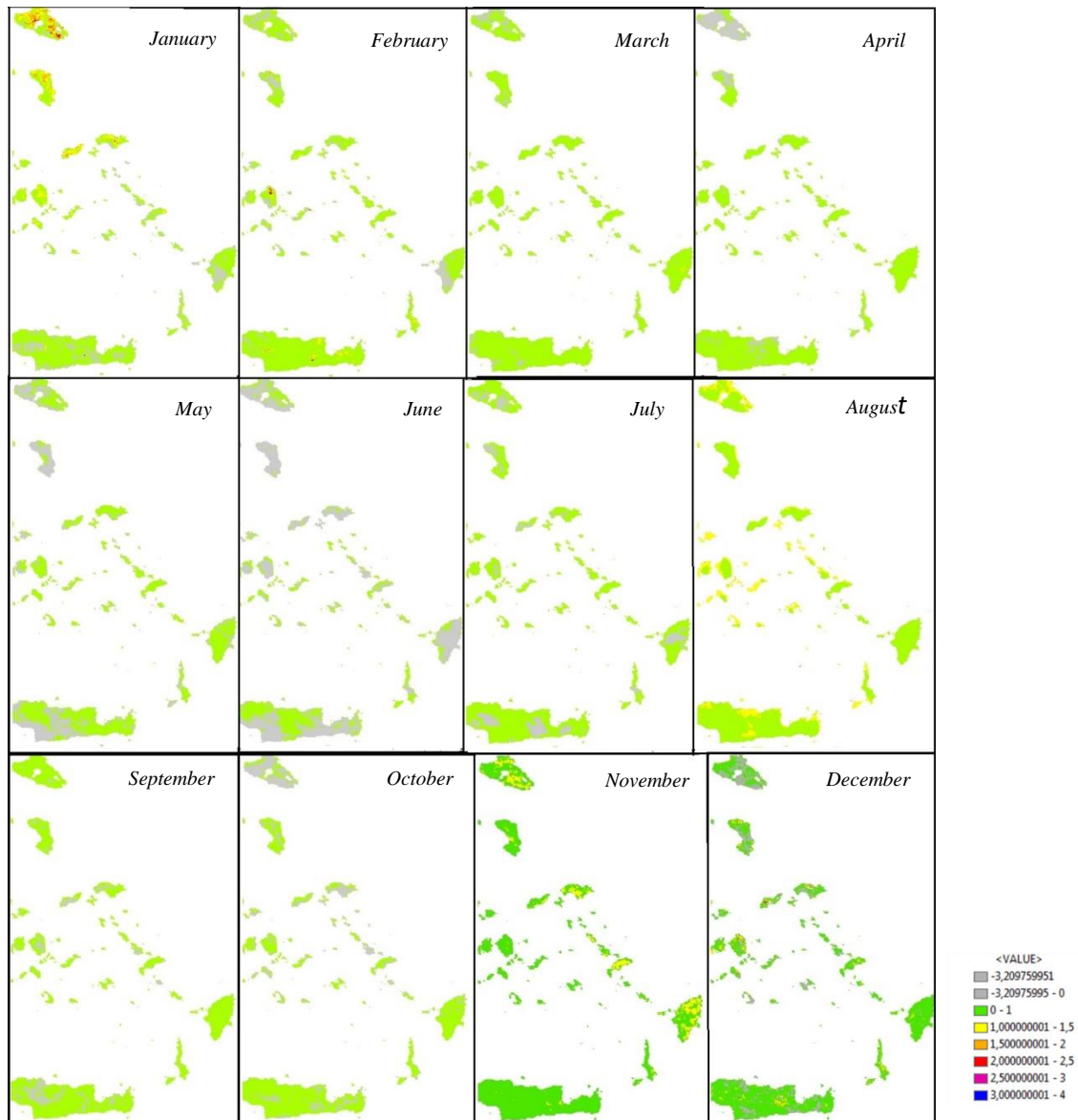
Fig. 25: Monthly ALICE maps for 2013

3.3.2: Daily Analysis

After the monthly investigation a daily approach followed for all the available data. The total mean and standard deviation are already calculated from the monthly investigation, so we only had to calculate the ALICE-RST index (equation 6) for each month of each year. A toolbox with the name "RETIRA_ALICE.tbx" (fig. 26) created in ModelBuilder for the calculation of both indexes (ALICE-RST & RETIRA).
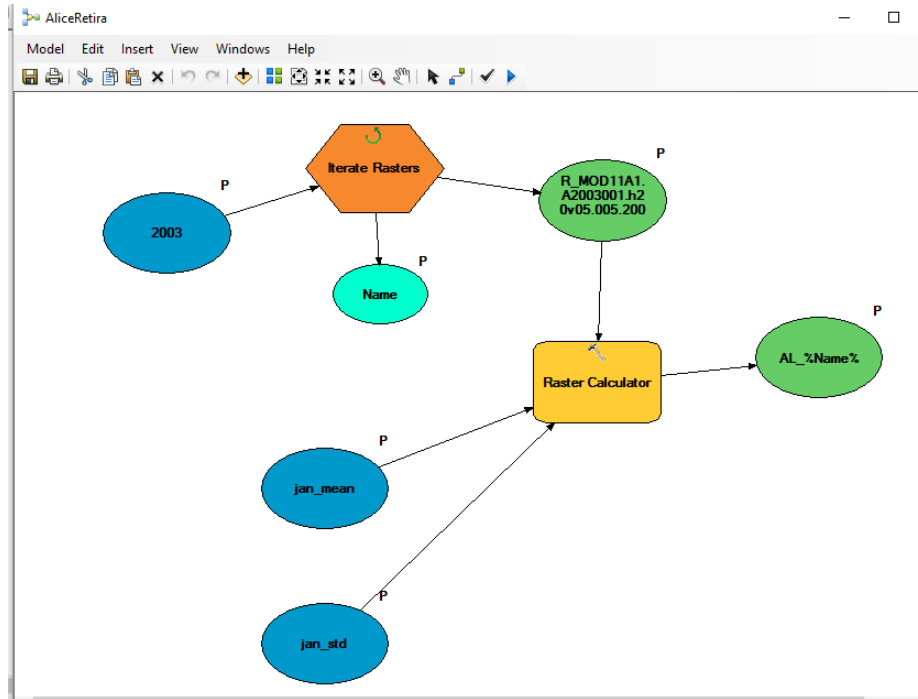
Fig. 26: The toolbox "RETIRA_ALICE" in ModelBuilder

A total of 4353 maps (table 7) created showing the TIR anomalies of the ALICE index.

3.4.: LST – RETIRA analysis

In order to get better results and as an opportunity to compare the algorithms on the TIR anomalies with MODIS-LST we decided to try the RETIRA index (equation 7) for the geothermal activity.

The $\Delta T(r,t')$ should be calculated for each pixel of each image before the determination of the new reference fields. For this reason a toolbox that is able to calculate the difference $\Delta T(r,t') = T(r,t')-T(t')$ created with the name "dT.tbx" (fig. 27). This new model determinates the difference between the current TIR signal value $T(x,y,t)$ measured at location r, and its spatial average $T(t)$, computed in place on the image at hand considering only cloud-free pixels, all belonging to the same, land or sea -according to where the r is located over the area-, class in the investigated area.
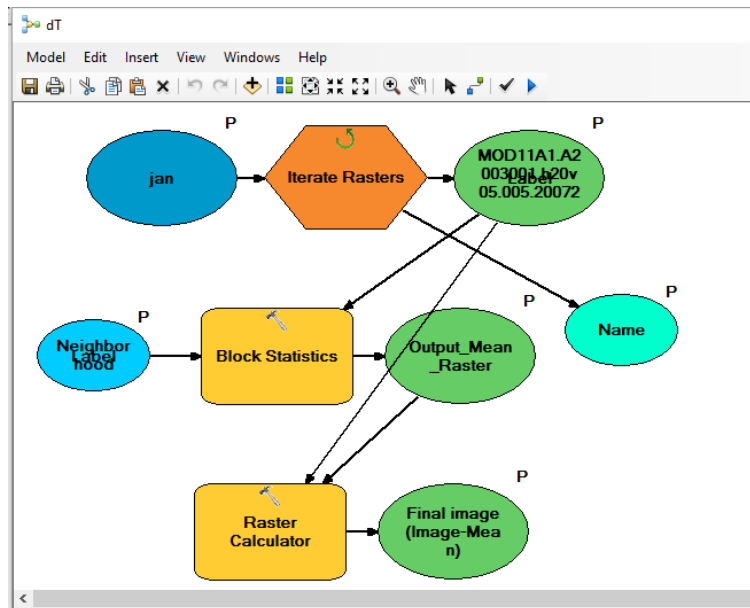
Fig. 27: The "dT.tbx" toolbox in ModelBuilder

The new reference fields calculated this time by using the "dT" images getting one map for each month (12 in total). The $\mu_{\Delta T}(r)$ and the $\sigma_{\Delta T}(r)$ of the index were computed for each month again with the use of the "cell_statistics" toolbox (fig. 22) and a monthly analysis followed by a daily investigation applied also for the RETIRA index.

3.4.1.: Monthly Analysis

By following the same procedure with the ALICE-RST index, a monthly analysis carried out with the use of the "cell_statistics" toolbox (fig. 22) for the creation of the temporal monthly mean and the use of the "raster_calculator" toolbox (fig. 23) for the calculation of the equation. 144 maps were produced before the daily imaging analysis. The comments of each observation will be discussed in the results.

3.4.2.: Daily Analysis

Again a daily analysis followed the previews step, and 4353 maps created this time with the calculation of RETIRA index. The difference is that this time there were used the "dT" images which we had already made before. The results of the images and the

comparisons between the RETIRA index and the ALICE-RST index, as well the comparison of the monthly and the daily analysis will be briefly discussed in the next chapter.

After each procedure a classification in the symbology needed to be done in order to recognize and classify the TIR anomalies with a signal greater than 2.5 ($\sigma < 2.5$). The toolbox "Symbology.tbx" (fig. 28) created in ArcGIS.
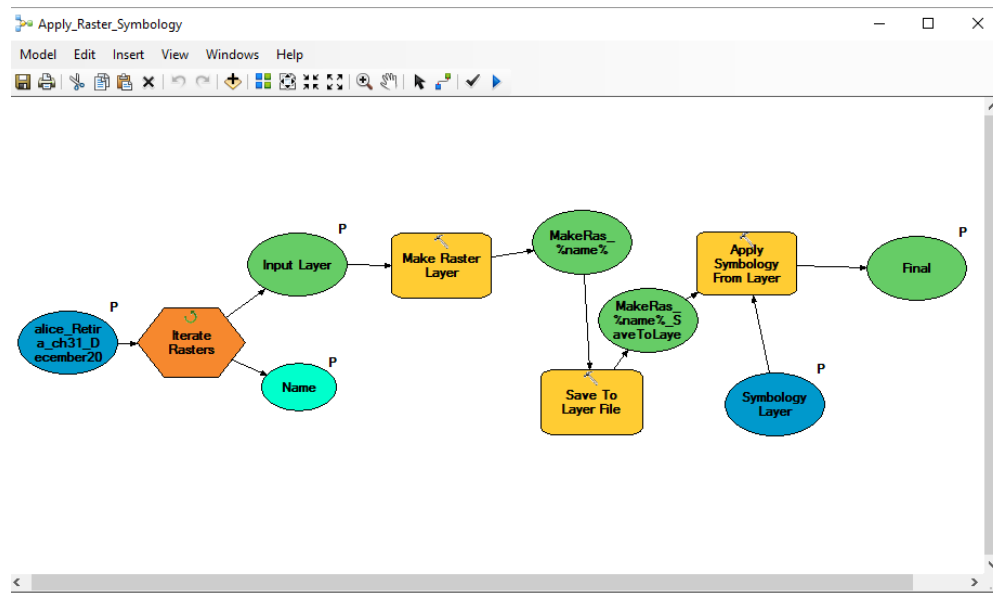
Fig. 28: The "symbology" toolbox opened in ModelBuilder

3.5: Problems of the method

The main problems that were observed are the following three;

- The cloud-coverage: Images that were taken from the satellite's sensor during nights with bad weather conditions, like high cloud-coverage and snow, had as result two problems; (i) no or false information can be found for the cloudy/snowy pixels and (ii) when the cloud-coverage is covering the biggest part of the image or of an area, many of the cloud-free pixels seems to be also affected and present false-true anomalies (fig. 29).

- inaccurate image navigation/co-location; since the chosen sensor, MODIS, is sun-synchronous a wrong navigation may cause intense TAs where sea pixels turn out to be erroneously co-located over land portions and because of this in

some daily images we observe a lot of false-true anomalous pixels especially on the coastlines (fig. 30).

- The amount of land; the area of interest for this Thesis consists only of islands, with the most of them being very small. The presence of extended lands (e.g. Turkey inland) within the images would affect the results in the smaller ones especially in the calculation of the reference fields and of the general mean and standard deviation values. For this reason we cut off at first the land of Turkey and Cyprus and followed the crop of Crete and Rhodes islands.
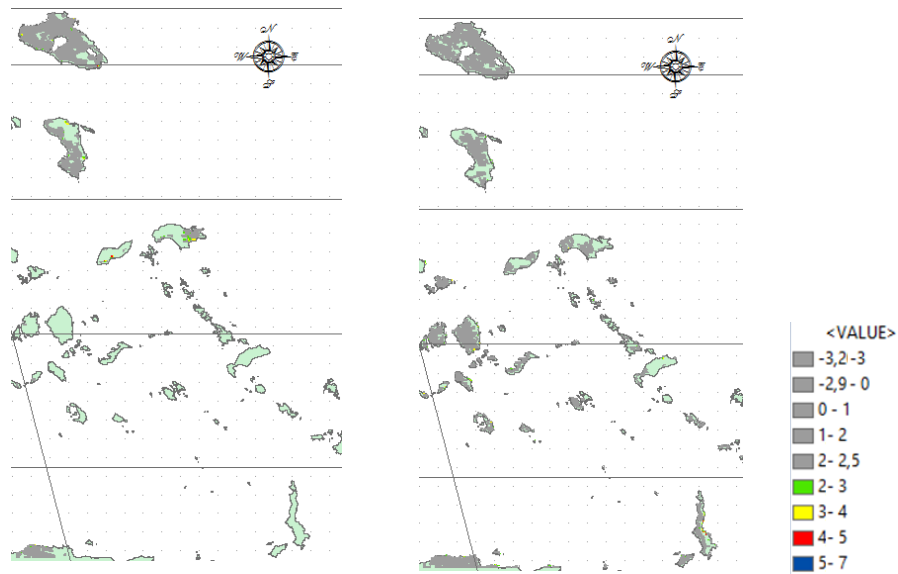
Fig.29: (b) 4/12/2012 (a) ?
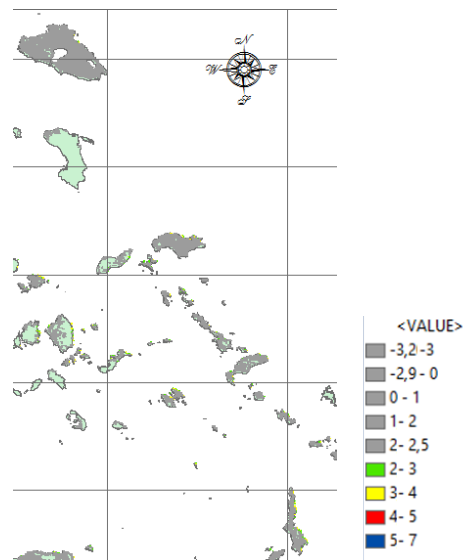
Fig.30: Map of 9/04/2003 showing anomalies due to image's inaccurate image navigation/co-location.

RESULTS

At first there are shortly represented the results of the comparison between the methods of ALICE-RST index and the RETIRA index, as well the results of the monthly and daily analysis in both of the applications.

- The temporally climate changes seemed to affect our images in the application of the ALICE-RST index and for this reason we moved on to the RETIRA index application. Indeed the weather effects seem to have disappeared. An example for the 5th of November of 2010 is represented bellow in the fig. 32.

- As it matters the monthly analysis we observed that in neither of the two indexes (eq. 6 and eq. 7) the anomalies are related with any phenomena, temporal or permanent and this is why we decided to further apply the daily analysis.

- On the contrary, the TIR anomalies in the daily analysis are observable in wide or smaller areas with true anomalies (related to natural phenomena like seismicity, geothermal activity and volcanic activity) or false-true anomalies (related to high cloud-coverage and inaccurate image navigation/co-location).

Thus, a more detailed investigation of the results on the daily images of the RETIRA-LST index took place. When the signal of a pixel is greater than 2.5 ($\sigma < 2.5$) it is considered as a TIR anomalous pixel. In the case of the daily analysis we had 1217 images out of the 4353 in total with a numerous of anomalous pixels. Since the signal could reach up to 3.5 ($\sigma < 3.5$), we made and used the "Symbology" toolbox that it is mentioned in the previous paragraph (fig. 28) with the classification on the right (fig. 31), in order to be able to observe the areas with the highest anomalies.
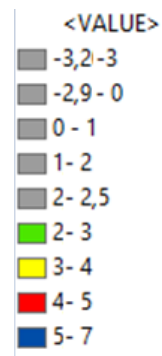
Fig.31: The classification of the RETIRA signal

From the 1217 images that had anomalous pixels the 318 are false alarms due to high cloud-coverage or inaccurate image navigation/co-location. In the rest 899 images a further investigation took place related to the seismicity. Using the site of "Institute of Geodynamics, National Observatory of Athens", a buffer zone of 150km were making around of each anomalous area for a time-period of 15 days before and 30 days after the anomalous areas for a magnitude greater than $3,8M_L$.
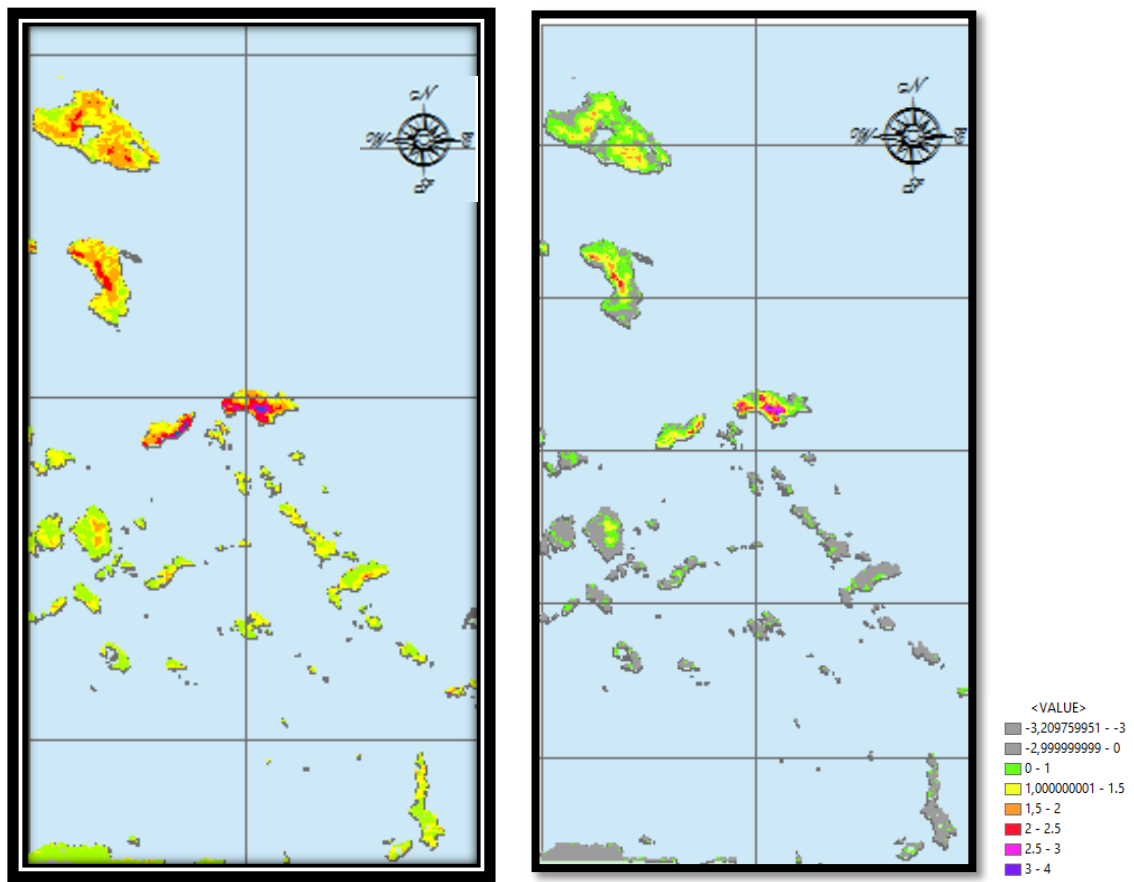
Fig. 32: (a) The map of 5/11/2010 created with the use of ALICE-RST index, (b) The map of 5/11/2010 created with the use of RETIRA-RST index
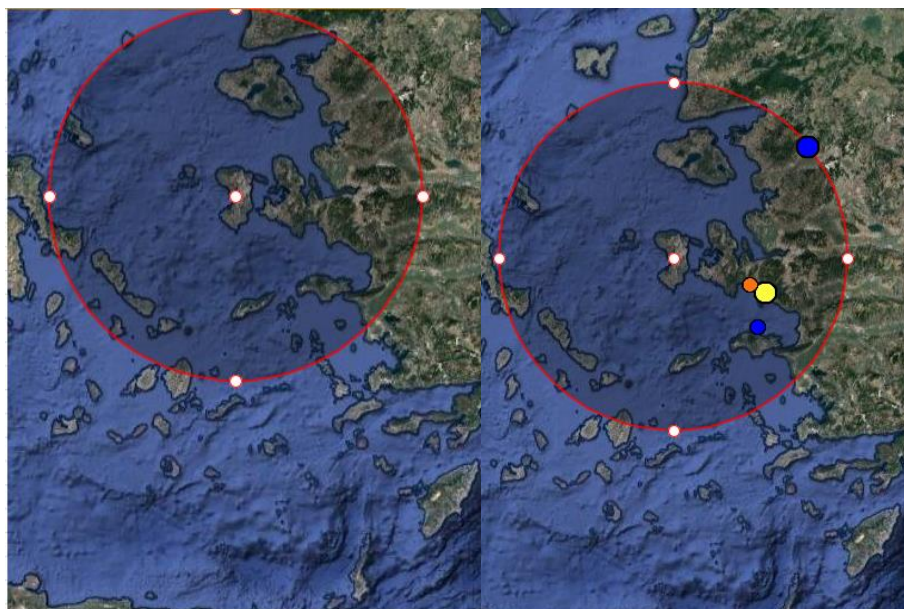
Fig. 33: Left: Example of anomalies that are not related to seismicity. Date 14/02/2014
Right: Example of anomalies that are related to seismicity. Date 25/01/2005

For better understanding, a presentation of the results will happen by referring to each area – island.

Nisyros Island
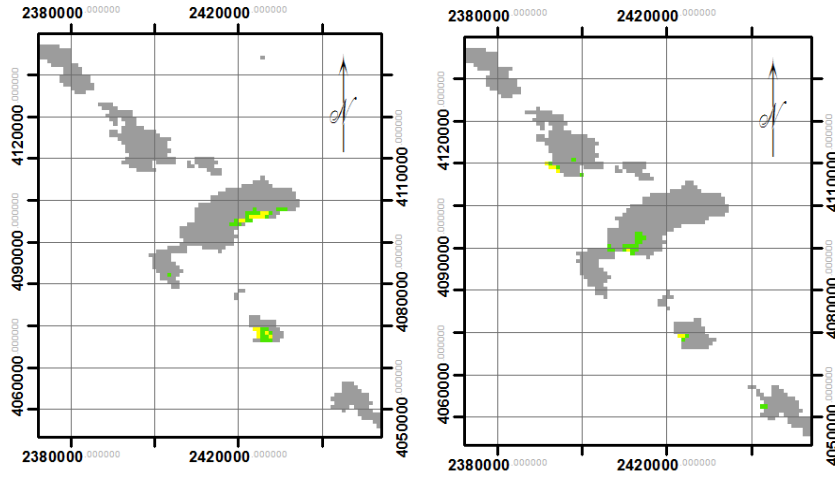
Fig. 33: (left) 28/09/2004   (right)

Santorini
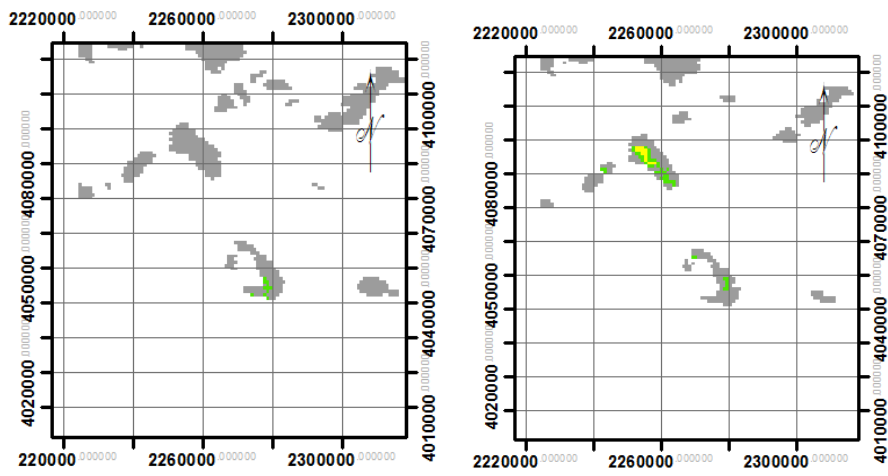
Fig. 35: (left) 27/8/2012   (right) 4/11/2014
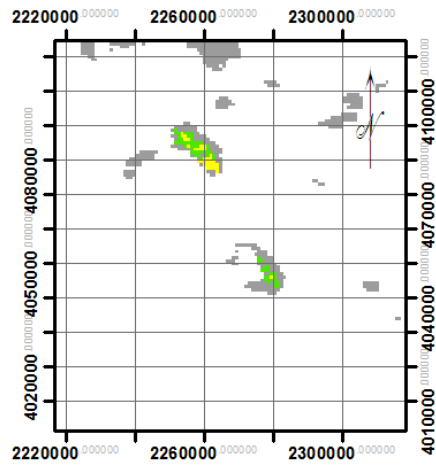
Fig. 36: 18/11/2014

Lesvos
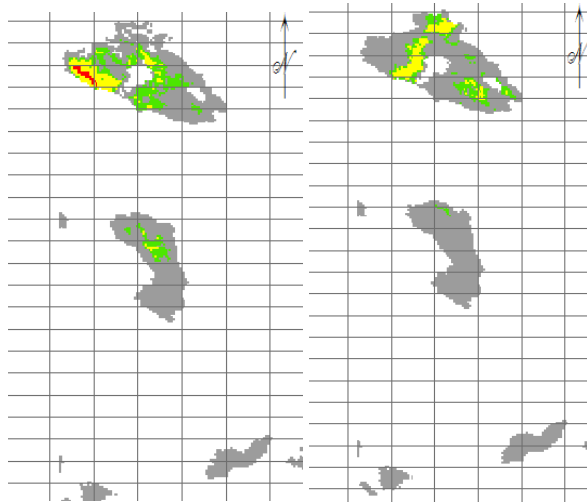
Fig. 37: (left) 10/11/2013   (right) 10/07/2007
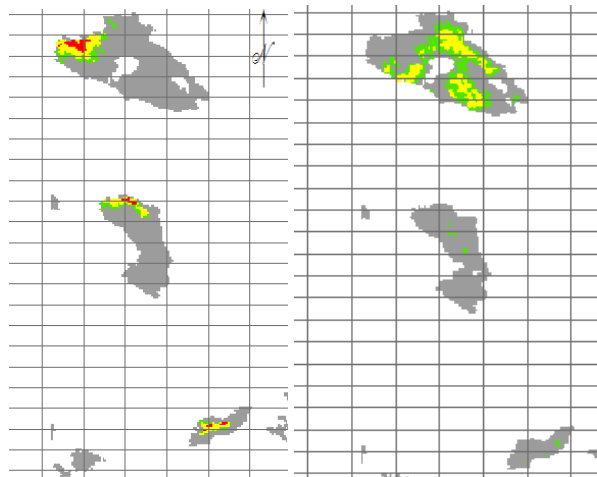
Fig. 38: (left) 20/07/2011 (right) 27/09/2012
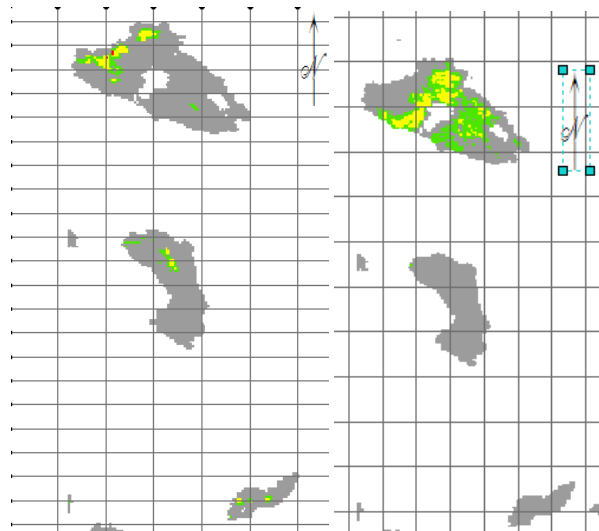
Fig. 39: (left) 13/09/2008   (right) 14/10/2014

Chios
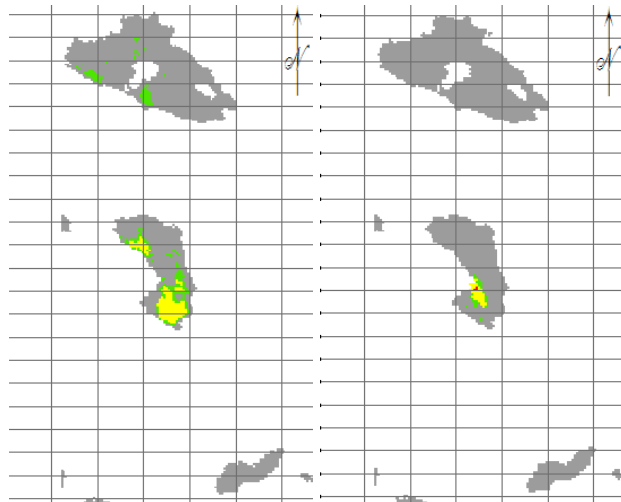
Fig. 40: (left) 16/11/2013   (right) 20/06/2012
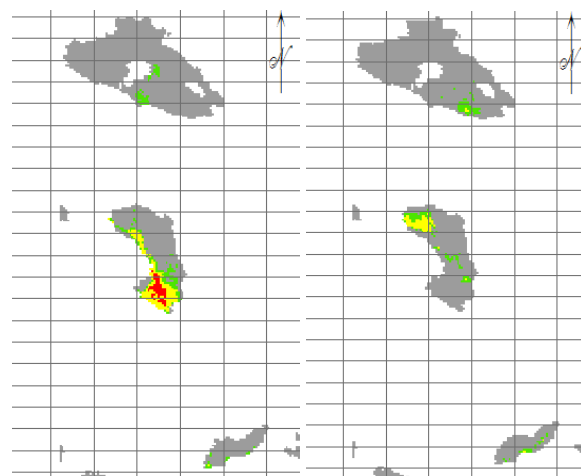
Fig. 41: (left)17/09/2011 (right) 29/09/2012
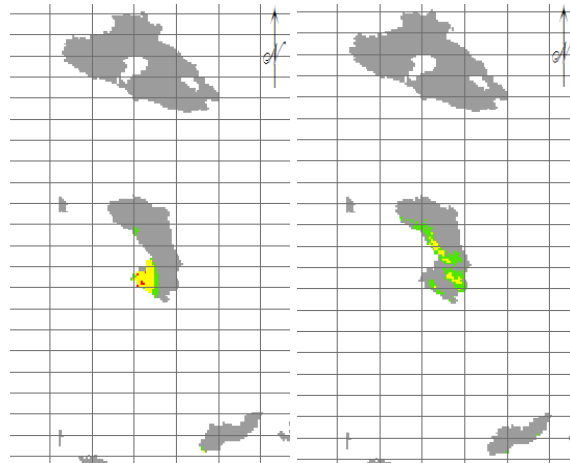
Fig. 42: (left) 21/08/2011 (right) 19/06/2012

Ikaria – Samos
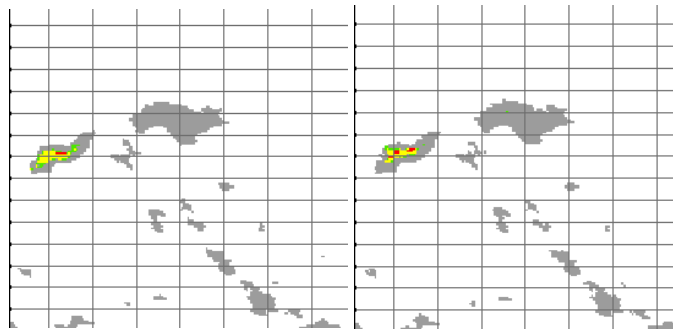
Fig. 43: (left) 5/08/2006 (right) 20/07/2011
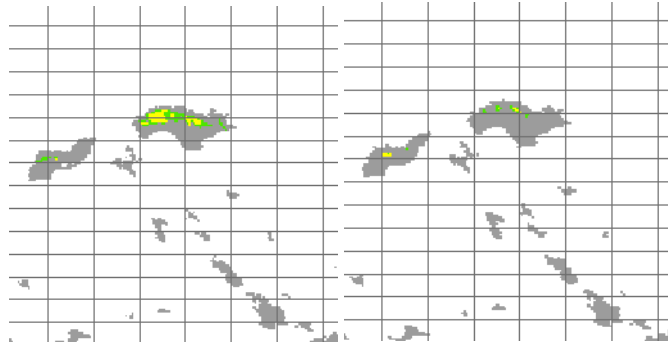
Fig. 44: (left) 05/10/2003   (right) 3/10/2004
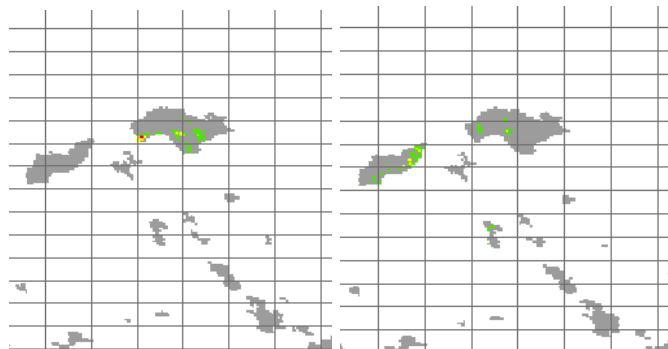
Fig. 45: (left) 16/11/2012   (right) 22/08/2008

Naksos
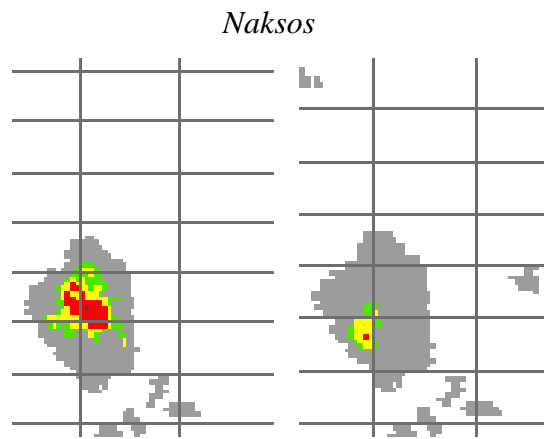
Fig.47: (left) 21/04/2008   (right) 20/05/2008

Integrating RST TIR results with geological data

After the integration of the RETIRA-LST results with the geological data of the study areas, a close spatial relationship of them was observed.

The thermal anomalies observed along the Dodecanese Province could be assigned to thermal ''remnant'' anomalies due to Miocene- Early Pliocene volcanism in the eastern Aegean-western Anatolia region.

The highest geothermal anomalies are observed in Lesvos and Chios islands. They are probably related to the thermal ''remnants'' of Miocene and more recent volcanism such as the volcanic activity along Asian Minor in Anatolia and Eastern Aegean Sea (e.g. Lesvos, Samothrace, Chios and Patmos). In the most cases of Lesvos Island, the thermal anomalies are coincided with the caldera rims (fig. X), while in some cases the anomalies are spatially correlated with major tectonic lineaments (fig. X).
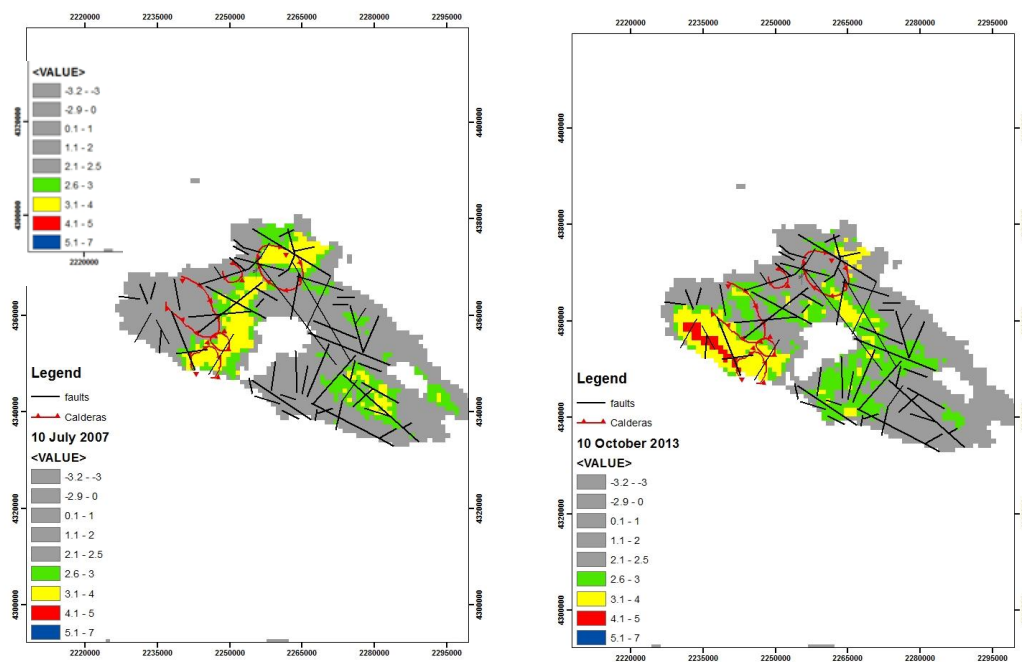
Fig. 48: Left: 10/07/2007 with the Geological map of Lesvos island, showing the faults and the caldera's of the island
Right: 10/10/2013 with the Geological map of Lesvos island, showing the faults and the caldera's of the island
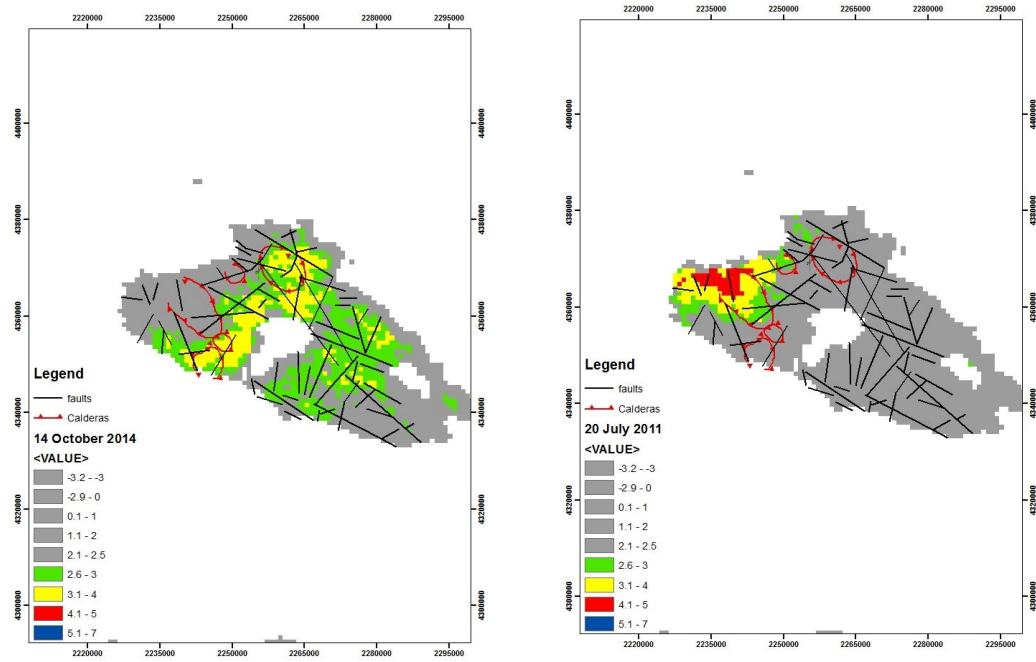
Fig. 49: Left: 14/10/2014 with the Geological map of Lesvos island, showing the faults and the caldera's of the island

Right: 20/07/2011 with the Geological map of Lesvos island, showing the faults and the caldera's of the island
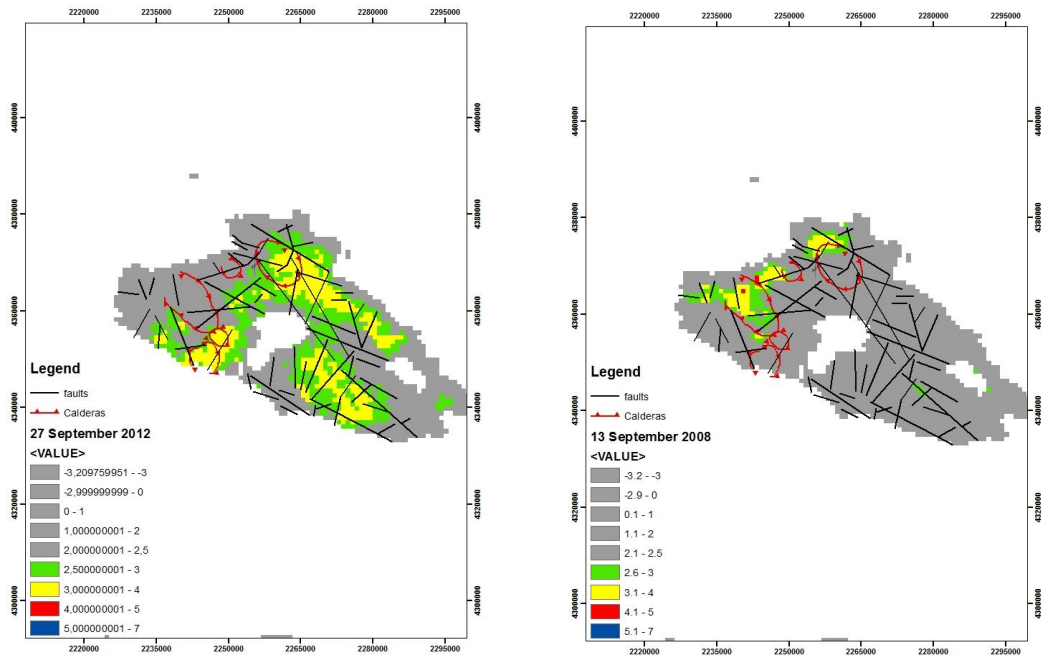
Fig. 50: Left: 27/09/2012 with the Geological map of Lesvos island, showing the faults and the caldera's of the island

Right: 12/09/2008 with the Geological map of Lesvos island, showing the faults and the caldera's of the island
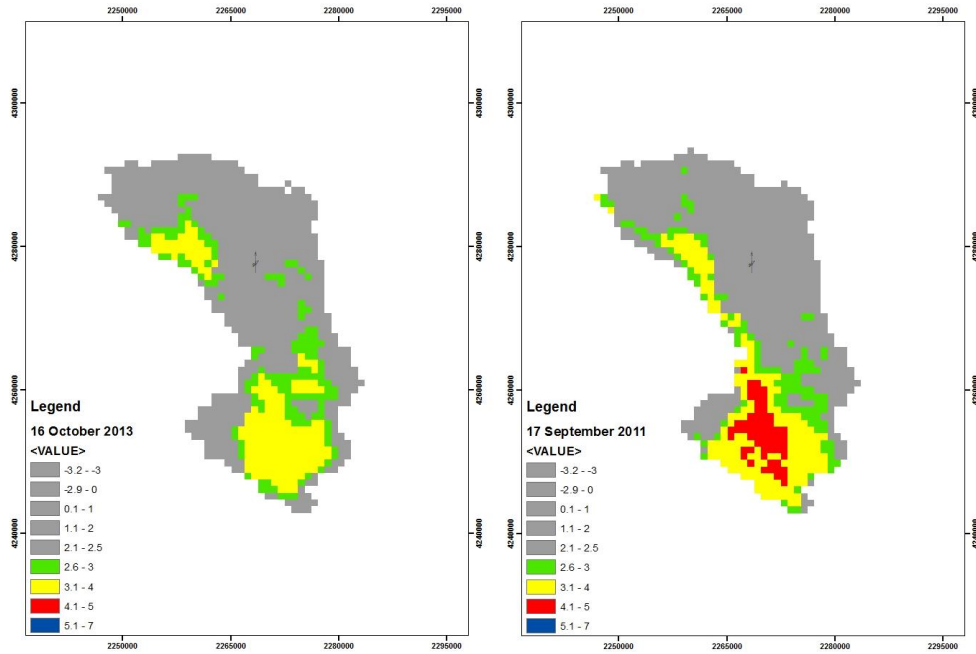
Fig. 51: Left: 18/10/2013

Right: 17/09/2011
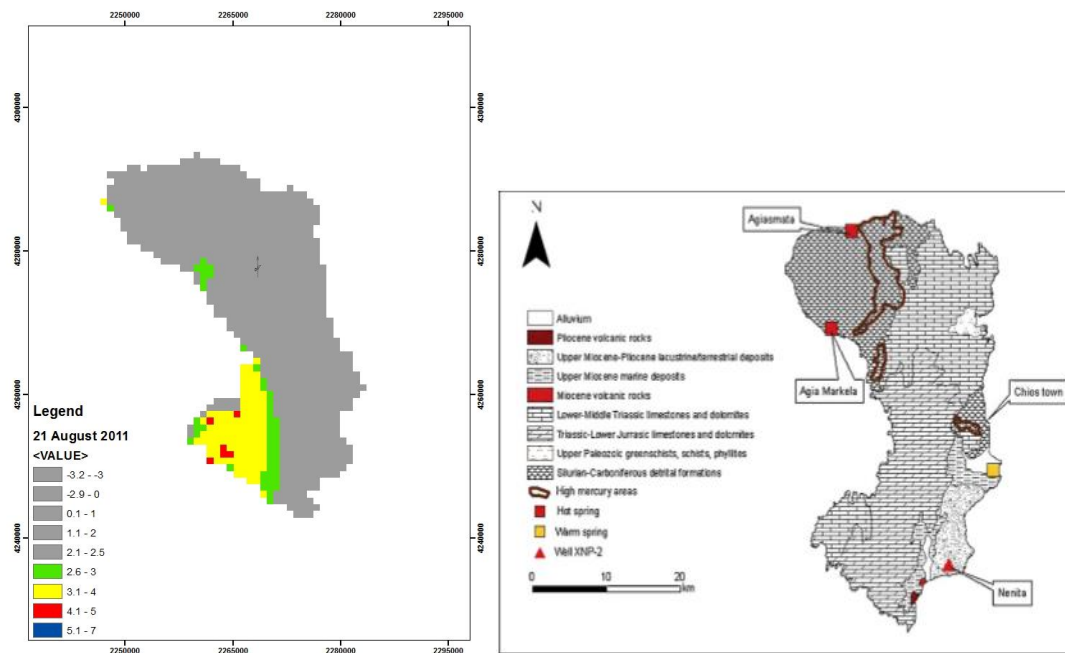
Fig. 52: Left: 21/08/2011

Right: Geologic map of Chios Island showing the location of thermal manifestations, shallow thermal wells, and areas with soils with high mercury concentrations.

Source: Exploring for geothermal resources in Greece, D. Mendrinos, I. Choropanitis, O. Polyzou, C. Karytsas

The pixels occupying the caldera of the volcano of Thera are interesting since they coincide with the volcano and the outflows (thermal springs) of the related geothermal field.
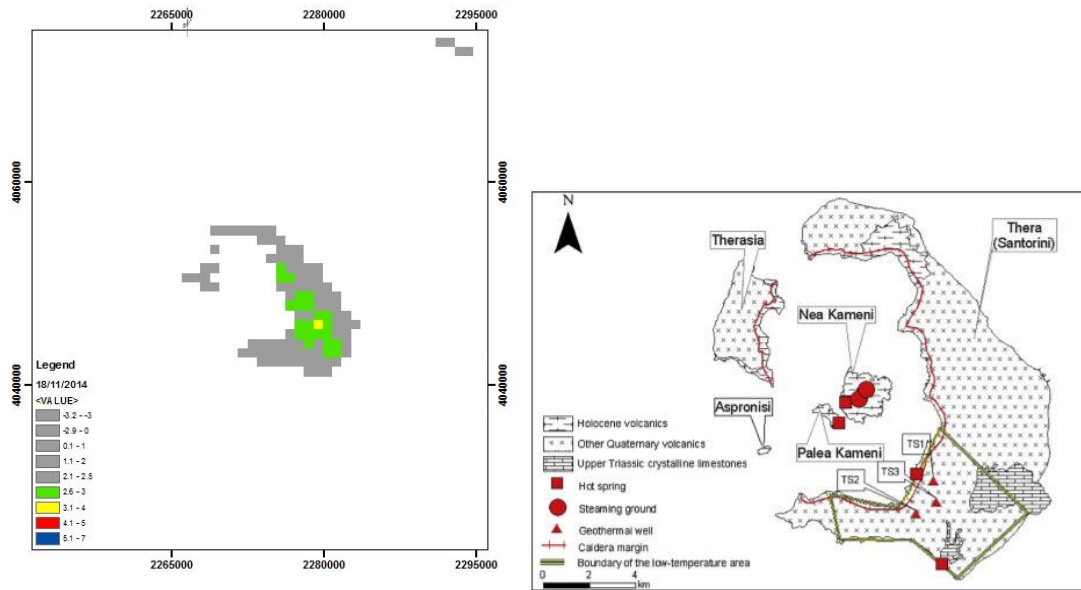
Fig. 53: Left: 18/11/2014

Right: Geological map of Santorini (Thira) archipelago showing the location of thermal manifestations, geothermal geothermal wells and likely extent of the low-temperature geothermal source.

Source: Exploring for geothermal resources in Greece, D. Mendrinos, I. Choropanitis, O. Polyzou, C. Karytsas

The thermal anomalies observed in central Cyclades are probably related to granodioritic plutons of Cyclades (see Naksos fig. 47).

The thermal anomalies mapped near the Kefalos gulf (Kos Plateau Tuff and Kefalos Tuff Ring volcanic products) in Kos Island probably represent another potential geothermal region which was characterized by Pliocene volcanic activity (Kos Plateau Tuff and Kefalos Tuff Ring eruptions) and the probable existence of the northern rim of an inundated caldera of a supervolcano (Allen 2001; Zouzias and St Seymour 2008). In Nisyros in most cases the thermal anomalies coincide with the hot springs, the steam vents and the pyroclastic crater that exist on the island (fig. 54)
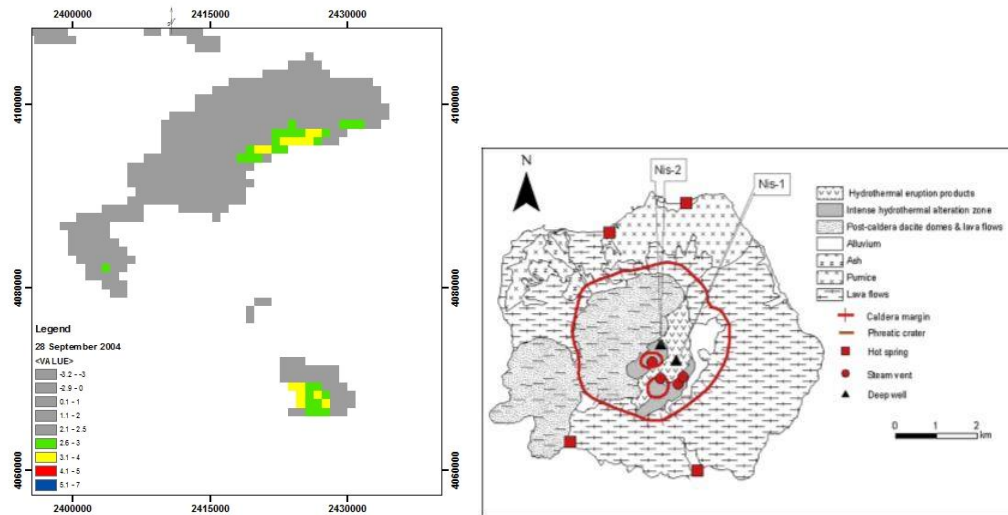
Fig. 54: Left: 28/09/2004

Right: Geologic map of Nisyros Island showing the location of the thermal manifestations and deep wells

Source: Exploring for geothermal resources in Greece, D. Mendrinos, I. Choropanitis, O. Polyzou, C. Karytsas

Conclusions

The existence of a geothermal field is related to volcanic activity and volcano-related phenomena such as calderas, thermal springs, and circulation of thermal waters. Identification of such thermal anomalies can be detected by Remote Sensing methods and verified by field measurements (Zougias, Miliaresis, Seymour, 2010).

In this Thesis a monitoring of the geothermal activity in the already known geothermal/volcanic fields of the Aegean Volcanic Arc and around it were implied by using Remote Sensing Techniques and MODIS – LST imagery. The selected area is the East Aegean Sea and the chosen period is 12 years from 2003 to 2014 with a total of 4353 daily images. For the detection of the TIR anomalies a change-detection algorithm called RST (Robust Satellite Technique) with the use of the ALICE (Absolutely Local Index of Change of the Environment) index compared with the RETIRA – LST index. For each of the indexes a monthly and a daily investigation took place.

For the daily results of the RETIRA-LST index we have;

- The RETIRA – LST index is able to reduce the affection of the temporal climate changes in the TIR anomalies in comparison with the ALICE-RST index that were tried in the first place.
- The monthly analysis in the case of those indexes is not able to detect the TIR anomalies.
- Out of the 4353 images in total the 1214 (35.7%) were found with anomalies, out of which the 339 (35.8%) are related to false alarms, like high cloud-coverage and…
- The rest 896 images include clear TIR anomalies. To secure that those anomalies are not related to seismicity a research took place with specific buffer zone (150km) around the areas, time-period before (15 days) and after (30 days) the anomalies and magnitude (< 3.8). By this way there were excluded other 614 maps that were totally related with seismicity.
- The number of the TIR anomalies related to geothermal activity <u>for each area</u> are;

    Chios: 129

Lesvos: 106

Naksos: 53

Samos: 38

Nisyros: 12

Kos: 13

Ikaria: 18

Santorini: 11

Ios: 17

Amorgos: 6

The thermal anomalies derived from the RST application in LST products identified:

(1) The highest geothermal anomalies are observed in Lesvos and Chios islands. They are probably related to the thermal ''remnants'' of Miocene and more recent volcanism such as the volcanic activity along Asian Minor in Anatolia and Eastern Aegean Sea. In the most cases of Lesvos Island, the thermal anomalies are coincided with the caldera rims, while in some cases the anomalies are spatially correlated with major tectonic lineaments.

(2) thermal anomalies mapped near the Kefalos gulf (Kos Plateau Tuff and Kefalos Tuff Ring volcanic products) in Kos Island probably represent another potential geothermal region which was characterized by Pliocene volcanic and the probable existence of the northern rim of an inundated caldera of a supervolcano. In Nisyros in most cases the thermal anomalies coincide with the hot springs, the steam vents and the pyroclastic crater that exist on the island.

(3) thermal anomalies of the Central Aegean which are related to the Thera volcano and its associated geothermal system and

(4) thermal anomalies associated with the granodioritic plutons of the Central Cyclades.

(5) thermal ''remnant'' anomalies of the Dodecanese Province to Miocene-Early Pliocene volcanism in the eastern Aegean western Anatolia region

The interpretation of geothermal anomalies from modern thermal remote sensing imagery and geological field data (e.g. geologic maps) provides new frontiers in the exploration of geothermal resources and volcanic fields.

Finally, the preliminary results of the applied method show a correlation of the revealed anomalies with the volcanic/geothermal activity and probably with the uplifting and circulation of the hydrothermal water through the radial and tectonic faults.

REFERENCE FIELDS

o *D. Zougias, George Ch. Miliaresis, K. St. Seymour, (2010), Probable Regional geothermal field reconnaissance in the Aegean region from modern multi-temporal night LST imagery, Environ Earth Sci*

o *D. Mendrinos, I. Choropanitis, O. Polyzou, C. Karytsas, (2009), Exploring for geothermal resources in Greece, Geothermics 39*

o *Zhao-Liang Li, Bo-Hui Tang, Hua Wu, Huazhong Ren, Guangjian Yan, Zhengming Wan, Isabel F. Trigo, Jose A. Sobrino, (2013), Satellite – derived land surface temperature: Current status and perspectives*

o *Ailsa Allaby, Michael Allaby, (1999), A dictionary for Earth Sciences*

o *Christopher J. Koroneos & Michael Fytikas, (1999), A potential of geothermal energy in Greece*

o *Mario-Cesar Suarez Arriaga, Fernando Samaniego V., Joshua Mendez Harper, (2010), Geothermal Reservoirs in Volcanic Islands, the Example of Santorini, Greece*

o *ομιλία Ακίνδυνου Κελεπερτζή, (2008)*

o *E. Dotsika, I. Leontiadis, D. Poutoukis, R. Cioni, B. Raco, (2006), Fluid Geochemistry of the Chios geothermal area, Chios island, Greece*

o *M. Fytikas, G. E. Vougioukalakis, (2005), The South Aegean Active Volcanic Arc: Present Knowledge and Future Perspectives*

o *Y. Antayhua-Vera, J. Lermo-Samaniego, L. Quintanar-Robles, O. Campos-Enriquez, (2015), Seismic activity and stress tensor inversion at Las Tres Virgenes Volcanic and Geothermal Field (Mexico), Journal of Volcanology and Geothermal Research, vol.305*

o *W. L. Friedrich, (2013), The Minoan Eruption of Santorini around 1613 B.C. and its consequences, TAGUNGEN DES LANDESMUSEUMS FOR VORGESCHICHTE HALLE, band 9*

o *Nomikou P., Bell K.L.C., Papanikolaou D., Livanos I., Martin J.F. et al., (2013), Exploring the Avyssos – Yali - Strogyli submarine volcanic complex at the eastern edge of the Aegean Volcanic Arc, Zeitschrift fur Geomorphologie, Supplementary Issues, vol.57, no.3*

o *Howari F.M, (2015), Prospecting for geothermal energy through satellite based thermal data: Review and the way forward, Global J. Environ. Sci. Manage., 276-274*

o *Zhengming Wan, (1999) MODIS Land-Surface Temperature Algorithm Theoretical Basis Document (LST ATBD),*

o *Zhengming Wan, (2006),* MODIS Land Surface Temperature Products User's Guide, Collection-5

o *H. S. Kinvig, A. Winson & J. Gottsman, (2010), Analysis of volcanic threat of Nisyros Island, Greece, with implications for aviation and population exposure, Natural Hazards and Earth System Sciences, 10*

o *C. Aliano, R. Corrado, C. Fizzola, N. Genzano, N. Pergola, V. Tramutoli, (2008), Robust TIR satellite techniques for monitoring earthquake active regions: limits, main achievements and perspectives, Annals of Geophysics, vol. 51*

o *M. Jin, Sh. Liang, (2006), An Improved Land Surface Emissivity Parameter for Land Surface Models Using Global Remote Sensing Observations, American Meteorological Society*

o *Cr. Madeira, Pr. Dash, F. Olesen, I. Trigo, Intercomparison of METEOSAT-8 derived LST with MODIS and AATSR similar products*

o *Ying Sun, Retrieval and Application of Land Surface Temperature, (2006)*

o *H. P. Heasler, D. Foley, (2009), Geothermal Systems and monitoring hydrothermal features, The Geological Society of America*

o *S. H. Potter, B. J. Scott, G. E. Jolly, V. E. Neall, D. M. Johnston, (2015), Introducing the Volcanic Unrest Index (VUI): a tool to quantify and communicate the intensity of volcanic unrest, Bulletin of Volcanology.*

o *G. Papadakis, F. Vallianatos, P. Sammonds, (2016), Non-extensive statistical physics applied to heat flow and the earthquake frequency-magnitude distribution in Greece, Physica A: Statistical Mechanics and its Applications, vol.456*

o *Mariano Lisi, (2010), Assessment of the exportability of the use of Robust Satellite Technique (RST) for seismic areas monitoring*

o *Alexander Eleftheriou, (2014), Robust Satellite Techniques (RST) for monitoring possible thermal anomalies related to seismic activity in Greece*

o *Paraskevi Tournaviti, (2013), Monitoring Crete Coastal sea-water quality by Remote Sensing Techniques*

o *J. Jiang, H. Li, Q. Liu, H. Wan, Y. Du, B. Cao, B. Zhong, S. Wu, (2015), Evaluation of Land Surface Temperature Retrieval from FY-3B/VIRR Data in an Arid Area of Northwestern China, Remote Sens. 2015*

o *Heasler, H. P., Jaworowski, C., & Foley, D. (2009). Geothermal systems and monitoring hydrothermal features. Geological Monitoring, 105-140.*

o *Baba, A., Bundschuh, J., & Chandrasekharam, D. (Eds.). (2014). Geothermal systems and energy resources: Turkey and Greece. CRC Press.*

o *Dickson, M.H.; Fanelli, M. What is Geothermal Energy? http://www.geothermal-energy.org/geo/geoenergy.phpIstituto di Geoscienze e Georisorse: Pisa, Italy, 2004. [Google Scholar]*

o *MUFFLER, P. and CATALDI, R., 1978. Methods for regional assessment of geothermal resources. Geothermics ,7, 53—89.*

o *Saemundsson, K. (2014). Geothermal systems in global perspective.001374011.*

o *Hochstein, M. P. (1990). Classification and assessment of geothermal resources. Small geothermal resources: A guide to development and utilization, UNITAR, New York, 31-57.*

o *Benderitter, Y., & Cormy, G. (1990). Possible approach to geothermal research and relative costs. Small geothermal resources: A guide to development and utilization, UNITAR, New York, 59-69.*

o *Lee, K. C. (2001). Classification of geothermal resources by exergy.Geothermics, 30(4), 431-442.*

o *Fytikas, M., Andritsos, N., Karydakis, G., Kolios, N., Mendrinos, D., & Papachristou, M. (2000). Geothermal exploration and development activities in Greece during 1995–1999. In Proceedings world geothermal congress (Vol. 2000, pp. 199-208).*

o *International Geothermal Association (2016). Available at https://www.geothermal-energy.org/*

o *Fytikas, M., Andritsos, N., Karydakis, G., Kolios, N., Mendrinos, D., & Papachristou, M. (2000, May). Geothermal exploration and development*

activities in Greece during 1995–1999. In Proceedings world geothermal congress (Vol. 2000, pp. 199-208).

o Fytikas, M., Andritsos, N., Dalabakis, P., & Kolios, N. (2005,). Greek Geothermal Update 2000-2004. In Proceedings World Geothermal Congress.

o R.G. Vaughan, H. Heasler, C. Jaworowski, J.B. Lowenstern, L.P. Keszthelyi. Provisional maps of thermal areas in Yellowstone National Park, based on satellite thermal infrared imaging and field observations U.S. Geol. Surv. Sci. Invest. Rep., 2014–5137 (2013) (22 p., http://dx.doi.org/10.3133/sir20145137)

o Gorny, V. I., Kritsuk, S. G., Latipov, I. S., & Tronin, A. A. (1997). Geothermal zoning of European Russia on the base of satellite infra-red thermal survey. In Proceeding of 30th Int Geological Congress, Beijing, China(Vol. 4, No. 14, pp. 63-80).

o Vaughan, RG; Keszthelyi, LP; Lowenstern, JB; Jaworowski, C; Heasler, H (2012). Use of ASTER and MODIS thermal infrared data to quantify heat flow and hydrothermal change at Yellowstone National Park. JOURNAL OF VOLCANOLOGY AND GEOTHERMAL RESEARCH, 233, 72-89.

o Mendrinos, D., Choropanitis, I., Polyzou, O., & Karytsas, C. (2010). Exploring for geothermal resources in Greece. Geothermics, 39(1), 124-137.

o Lund, J. W., & Boyd, T. L. (2016). Direct utilization of geothermal energy 2015 worldwide review. Geothermics, 60, 66-93.

o Andritsos, N., Dalambakis, P., Arvanitis, A., Papachristou, M., & Fytikas, M. (2015). Geothermal developments in Greece—country update 2010–2014. In Proceeding, World Geothermal Congress (p. 11)

o Geothermal Energy Association (2016). http://geo-energy.org/pdf/Geothermal_Energy_and_Induced_Seismicity_Issue_Brief.pdf

o Cladouhos, T., Petty, S., Foulger, G., Julian, B., & Fehler, M. (2010). Injection induced seismicity and geothermal energy. GRC Transactions, 34, 1213-1220.

o *Majer, E. L., & Peterson, J. E. (2007). The impact of injection on seismicity at The Geysers, California Geothermal Field. International Journal of Rock Mechanics and Mining Sciences, 44(8), 1079-1090.*

o *Hubbert, M. K., & Rubey, W. W. (1959). Role of fluid pressure in mechanics of overthrust faulting I. Mechanics of fluid-filled porous solids and its application to overthrust faulting. Geological Society of America Bulletin, 70(2), 115-166.*

o *Yang, F., Zhen, H., Jiang, T., Li, Y. Q., & Gong, C. (1999). Thermal infrared remote sensing of geothermal resource. In SPIE's International Symposium on Optical Science, Engineering, and Instrumentation (pp. 264-272). International Society for Optics and Photonics.*

o *Clark, R. N. (1999). Spectroscopy of rocks and minerals, and principles of spectroscopy. Manual of remote sensing, 3, 3-58.*

o *Martini, B. A., Hausknecht, P., Pickles, W. L., & Cocks, P. A. (2004). The northern Fish Lake Valley pull-apart basin: geothermal prospecting with hyperspectral imaging. Geothermal Resources Council Transactions, 28, 663-667.*

o *Littlefield, E. F., & Calvin, W. M. (2014). Geothermal exploration using imaging spectrometer data over Fish Lake Valley, Nevada. Remote Sensing of Environment, 140, 509-518.*

o *Hellman, M. J., & Ramsey, M. S. (2004). Analysis of hot springs and associated deposits in Yellowstone National Park using ASTER and AVIRIS remote sensing. Journal of Volcanology and Geothermal Research, 135(1), 195-219.*

o *Vaughan, R. G., Hook, S. J., Calvin, W. M., & Taranik, J. V. (2005). Surface mineral mapping at Steamboat Springs, Nevada, USA, with multi-wavelength thermal infrared images.Remote Sensing of Environment, 99(1), 140-158.*

o *Fred G.R., Watson R.E., Lockwood W.B., Newman T.N., Anderson R.A.G. (2008) - Development and comparison of Landsat radiometric and snowpack model inversion techniques for estimating geothermal heat flux. Remote Sensing of Environment, 112 (2): 471-481. doi: http://dx.doi.org/10.1016/j.rse.2007.05.010*

o *Patrick, M., Dean, K., & Dehn, J. (2004). Active mud volcanism observed with Landsat 7 ETM+. Journal of Volcanology and Geothermal Research, 131(3), 307-320.*

o *Miliaresis, G. (2012a). Elevation, latitude/longitude decorrelation stretch of multi-temporal LST imagery Photogrammetric Engineering & Remote Sensing 87:2.151-160*

o *Miliaresis, G. (2012b). Selective variance reduction of multi-temporal LST imagery in the East Africa Rift System Earth Science Informatics 5:1.1-12.*